

## Testing models of accreting stars in massive binaries on $\zeta$ Ophiuchi

M. RENZO<sup>1,2</sup> AND Y. GÖTBERG<sup>3</sup>

<sup>1</sup>*Department of Physics, Columbia University, New York, NY 10027, USA*

<sup>2</sup>*Center for Computational Astrophysics, Flatiron Institute, New York, NY 10010, USA*

<sup>3</sup>*The Observatories of the Carnegie Institution for Science, 813 Santa Barbara Street, Pasadena, CA 91101, USA*

### ABSTRACT

Most massive stars are born in binary systems close enough for mass-transfer episodes. These modify the appearance, internal structure, and future evolution of both stars. However, self-consistent models of the accretors are rare. The nearest O-type star to Earth,  $\zeta$  Ophiuchi, has long been proposed to have accreted mass from a former companion, before being ejected at the time of the companion’s supernova explosion. Therefore, this star provides an ideal test bed for models of accretors in binaries. We use MESA to model the evolution of a massive binary evolving through a stable mass transfer after the donor’s main sequence (case B, initial period 100 days). Adopting common assumptions for the treatment of rotation, chemical mixing, and mass transfer efficiency, our models of the accreting star reproduce reasonably well the kinematic, spectroscopic, and photometric properties of  $\zeta$  Ophiuchi. We compare the internal structure and evolution of our accretor to fast-rotating single stars, and find that the late and extreme spin up by binary interactions yields, at the end of the main sequence, a faster-spinning core in the accretor than in rotating single stars. Our models demonstrate the impact of mass accretion on the secondary star in a binary, with possible implications for its further evolution (either in a binary or as single stars), the final collapse, and the resulting spins of the compact object formed.

*Keywords:* stars: individual:  $\zeta$  Ophiuchi – stars: massive – stars: binaries

### 1. INTRODUCTION

The overwhelming majority of massive stars is born in multiple systems (e.g., Mason et al. 2009; Almeida et al. 2017), and a large fraction will exchange mass or merge with a companion in their lifetime (e.g., Sana et al. 2012). The most common type of interaction is a stable mass transfer through Roche Lobe overflow (RLOF) after the end of the donor’s main sequence (case B, Kippenhahn & Weigert 1967). Many studies have focused on the dramatic impact these interactions have on the donor star (e.g., Morton 1960; Yoon et al. 2017; Götberg et al. 2017, 2018; Laplace et al. 2020, 2021; Blagorodnova et al. 2021). Often the binary companion is treated as a point mass.

#### 1.1. The importance of accretor stars

However, binary interactions have a crucial impact on the initially less massive star: during mass transfer, these are expected to accrete mass, spin-up to critical rotation (e.g., Packet 1981), and possibly be polluted by nuclearly processed material from the inner core of the donor star (e.g., Blaauw 1993). The growth of the convective core due to the increased mass leads to “reju-

venation” of the accretor (e.g., Neo et al. 1977; Schneider et al. 2016).

Understanding the evolution of accretors in massive binaries has wide and crucial implications for stellar populations, electromagnetic transient observations, and gravitational-wave progenitors.

Accretors (and merger products) can appear as blue stragglers (e.g., Chen & Han 2009, 2010; Rain et al. 2021) and thus impact cluster populations, their age estimates, and their main sequence morphology (e.g., Pols & Marinus 1994; Wang et al. 2020). The high spin of the accretor post-mass-transfer might be the dominant explanation for the origin of hydrogen (H) rich massive stars showing emission lines (e.g., Bodensteiner et al. 2020; Vinciguerra et al. 2020). Rotationally-mixed accreting star at low metallicity might also be important for the ionizing flux of high-redshift galaxies (e.g., Eldridge & Stanway 2012).

The majority of massive binaries will be disrupted by the first supernova ejecting the companion (“binary SN scenario”, Blaauw 1961; De Donder et al. 1997; Eldridge et al. 2011; Boubert & Evans 2018; Renzo et al. 2019; Evans et al. 2020). Therefore, populations of field massive stars contain presently single O-type stars that ac-

creted mass earlier on. A small fraction would be sufficiently fast to become runaway stars, but the majority of these will be too slow to stand out in astrometric surveys. Assuming a constant star formation history, Renzo et al. (2019) estimated that  $10.1^{+4.6\%}_{-8.6\%}$  ( $0.5^{+2.1\%}_{-0.5\%}$ ) of O-type stars could be slow “walkaway” (runaway) accretors ejected after the companion’s SN explosion.

From the transients perspective, massive accretor stars are also important: Zapartas et al. (2019) showed that  $14^{+4\%}_{-11\%}$  of H-rich (type II) SNe might come from progenitors ejected from a binary after the explosion of their companion. The fact that they accreted mass before exploding can influence their helium (He) core mass and thus the explosion properties and the inferred progenitors (Zapartas et al. 2021). The high post-mass transfer rotation rate of accretor stars in binaries might have implications for the formation of long gamma-ray burst progenitors (e.g., Cantiello et al. 2007).

Finally, the majority of isolated binary evolution scenarios for gravitational-wave progenitors include a common-envelope phase. This is initiated by the originally less massive accretor, after the formation of the first compact object (e.g., Belczynski et al. 2016; Tauris et al. 2017; Broekgaarden et al. 2021). Therefore, it is possible that accretion of mass before the formation of the first compact object could modify the internal structure of the star that will initiate the common-envelope (e.g., Law-Smith et al. 2020; Klencki et al. 2021). Specifically, the rotation rate, chemical composition, and innermost structure of the envelope (because of rejuvenation) might differ from a single star.

Despite their importance, accretor stars in binaries have so far received much less attention than the donor stars, with the pioneering studies of Ulrich & Burger (1976); Hellings (1983, 1984), and Braun & Langer (1995) as notable exceptions. Large grids of accretor models are lacking, most of the studies focus on lower mass systems (e.g.,  $M_1 \lesssim 16 M_\odot$  in van Rensbergen et al. 2011) or neglect the crucial impact of rotation (e.g., Sravan et al. 2019, but see also Wang et al. 2020) and only few sparse massive models exist (e.g., Cantiello et al. 2007).

This is because of the difficulty of modeling accretor stars, which requires following in detail the coupled evolution of two rotating stars exchanging mass. Moreover, the admittedly large number of free parameters involved in the modeling of each individual star and their interactions makes robust predictions challenging to obtain. We emphasize that rapid population synthesis calculations typically cannot include the effects of binary mass transfer on the internal structure of the stars, and rely on the implicit assumption that the accretor is suffi-

ciently well described by a (possibly fast-rotating) single star model.

## 1.2. A prototypical example of accretor: $\zeta$ Ophiuchi

Here, we argue that the nearest O-type star to Earth,  $\zeta$  Ophiuchi<sup>1</sup> ( $\zeta$  Oph) provides a unique opportunity to constrain these models.  $\zeta$  Oph has a distance from Earth of  $107 \pm 4$  pc (Neuhäuser et al. 2020, and references therein), and a spectral type O9.5IVnn (Sota et al. 2014). It occasionally shows emission lines, making it an Oe star (Walker et al. 1979; Vink et al. 2009). Its surface rotation rate is extremely large, with most estimates of the projected rotational velocity from optical spectra exceeding  $v \sin(i) \gtrsim 400$  km s<sup>-1</sup> (corresponding to the “nn” in the spectral type, e.g., Zehe et al. 2018). Using optical interferometry, Gordon et al. (2018) were able to measure the centrifugal distortion of  $\zeta$  Oph, suggesting close-to-breakup rotation. By comparing the observed  $v \sin(i)$  to the theoretical breakup rotation, Zehe et al. (2018) also constrained the inclination angle to  $i \gtrsim 56$  degrees.

$\zeta$  Oph was originally identified as a runaway because of its large proper motion by Blaauw (1952). Unfortunately, the *Gaia* data for this object are not of sufficient quality<sup>2</sup> to improve previous astrometric results, but estimates of the peculiar velocity range in  $30 - 50$  km s<sup>-1</sup> (e.g., Zehe et al. 2018; Neuhäuser et al. 2020). The large velocity with respect to the surrounding interstellar material is also confirmed by the presence of a prominent bow-shock (e.g., Bodensteiner et al. 2018).

Because of its young apparent age, extremely fast rotation, and nitrogen (N) and He rich surface (e.g., Herrero et al. 1992; Blaauw 1993; Villamariz & Herrero 2005; Marcolino et al. 2009),  $\zeta$  Oph is a prime example of the outcome of the binary SN scenario (Blaauw 1993). Many studies have suggested  $\zeta$  Oph might have accreted mass from a companion before acquiring its large velocity, both from spectroscopic and kinematic considerations (e.g., Blaauw 1993; Hoogerwerf et al. 2000, 2001; Tetzlaff et al. 2010; Neuhäuser et al. 2020) and using stellar modeling arguments (e.g., van Rensbergen et al. 1996). Recently, Neuhäuser et al. (2020) suggested that  $1.78 \pm 0.21$  Myr ago a supernova (SN) in Upper-Centaurus-Lupus produced the pulsar PSR B1706-16, ejected  $\zeta$  Oph, and also injected the short-lived radioactive isotope  $^{60}\text{Fe}$  on Earth. This argues strongly for a successful SN explosion of the companion with a large  $\sim 250$  km s<sup>-1</sup> natal kick, which in most cases would be

<sup>1</sup> also known as HD 149 757.

<sup>2</sup> The renormalized unit weighted error (RUWE) of this star in *Gaia* EDR3 is 4.48.

sufficient to disrupt the binary (e.g., Tauris 2015; Renzo et al. 2019; Evans et al. 2020).

Although the nature of  $\zeta$  Oph as a binary product is well established, because of its observed large surface rotation rate, previous attempts to model it rely purely on rotational mixing to explain the N- and He-rich surface composition (e.g., Maeder & Meynet 2000). Even the binary models of van Rensbergen et al. (1996) assumed rotational mixing from the inside of the accreting star driven by the spin-up during mass transfer (see also Cantiello et al. 2007). However, Villamariz & Herrero (2005) (hereafter, VH05) were unable to find good fit for the stellar spectra using the single-star rotating models from Meynet & Maeder (2000, 2003): by the time rotational mixing enriches the surface, single massive stars have significantly spin down through wind mass loss.

This may not be surprising: algorithms modeling rotational mixing predict lower efficiency for metal-rich and relatively low mass stars. The reason is the increased importance of mean molecular weight gradients and the longer thermal timescales compared to more massive stars (e.g., Yoon et al. 2006; Perna et al. 2014). The parent association of  $\zeta$  Oph has a metallicity  $Z = 0.01 \simeq Z_\odot$  (based on asteroseismology from Murphy et al. 2021), and mass estimates for  $\zeta$  Oph range from  $13 - 25 M_\odot$ , at the lower end of the range where efficient mixing might bring He and CNO-processed material to the surface (chemically homogeneous evolution, Maeder & Meynet 2000).

Given the challenges in explaining the surface composition of  $\zeta$  Oph as a rotating single star and the strong evidence for its past as a member of a binary system, this star offers a unique opportunity to constrain the evolution of accreting stars in massive binary systems.

Here, we present self-consistent binary evolution models for  $\zeta$  Oph computing simultaneously the coupled evolution of *both* donor and accretor star and their orbit. After describing our MESA setup in Sec. 2, we show our best model which reproduces the majority of the salient features of this star in Sec. 3. We discuss the sensitivity of our results to the admittedly many free parameters required for this kind of computations in Sec. 4. Finally, we conclude in Sec. 5.

## 2. MODELING MASSIVE BINARIES WITH MESA

Modeling the evolution of massive binaries ( $M_1 \gtrsim 20 M_\odot \geq M_2$ ) is challenging because of the intricate role of several notoriously difficult stellar physics ingredients (accretion, differential rotation, mixing, high mass-loss rates, etc.). We follow self-consistently the coupled evolution of two massive stars in a binary system using MESA (version 15140, Paxton et al. 2011, 2013, 2015, 2018,

2019). Our choice of input parameters and our numerical results are available at [10.5281/zenodo.4701565](https://doi.org/10.5281/zenodo.4701565). We discuss here only the main relevant physical parameters and describe tests changing some of the fiducial values in Sec. 4. Appendix A gives more details on our choice of input physics, and appendix B discuss the numerical resolution in space and time.

We adopt the Ledoux criterion to determine convective stability and a mixing length parameter of 1.5. We include semiconvection and thermohaline mixing following Langer et al. (1983) and Kippenhahn et al. (1980), respectively, each with efficiency 1.0. We use the exponential core overshooting from Herwig (2000) with free parameters  $(f, f_0) = (4.25 \times 10^{-2}, 10^{-3})$  (Claret & Torres 2017) which broadly reproduce the width of the main sequence from Brott et al. (2011). We also use the local implicit enhancement of the convective flux in superadiabatic regions (MLT--) introduced in MESA 15140.

We treat rotation in the “shellular” approximation (e.g., Zahn 1992; Ekström et al. 2012), that is we assume constant rotational frequency  $\omega$  along isobaric surfaces. Furthermore, we assume tidal synchronization at zero age main sequence (ZAMS) – the beginning of our runs. For our fiducial period choice ( $P = 100$  days), this means the stars are initially slow rotators: the surface averaged rotational velocity is  $\lesssim 3 \text{ km s}^{-1}$  for both. Our models include a diffusive approximation for meridional currents (Eddington-Sweet circulations, (Sweet 1950)), which dominate the chemical mixing due to rotation. We also include the secular and dynamical shear instabilities, and the Goldreich-Schubert-Fricke instability, but these remain subdominant throughout the evolution of our models. We assume a Spruit-Tayler dynamo for the transport of angular momentum (Spruit 2002), and chose the same free parameters as Heger et al. (2000). This also includes the implicit rotational enhancement of wind mass loss to keep the rotation sub-critical as in Langer (1998). Specifically, at each timestep we calculate a wind enhancement factor to reduce the ratio  $\omega/\omega_{\text{crit}} \lesssim 0.95$  where  $\omega_{\text{crit}} = \sqrt{(1 - L/L_{\text{Edd}})GM/R^3}$  and  $L_{\text{Edd}}$  is the Eddington luminosity computed using the stellar opacity down to optical depth  $\tau = 2/3$ ,  $L$  is the luminosity,  $R$  the radius, and  $G$  the gravitational constant. However, we allow a tolerance of 0.05 on this limit.

We assume a fiducial metallicity of  $Z = 0.01$  informed by the present-day  $Z$  of the parent cluster (Murphy et al. 2021), and assume solar scaling of the relative element abundances (Grevesse & Sauval 1998). We include wind mass loss following Vink et al. (2000, 2001) for effective temperature  $T_{\text{eff}} \gtrsim 10^{4.2} \text{ K}$ , and de Jager et al. (1988) for  $T_{\text{eff}} \lesssim 10^{4.2} \text{ K}$ , both with a scaling fac-

tor of 1. Nominally, this means our wind mass-loss rate post-mass transfer is overestimated by almost a factor of 100 compared to observations (weak wind problem, see Marcolino et al. 2009). However, Lucy (2012) and Lagae et al. (2021) proposed that the temperature structure of the winds of low-luminosity O-type stars might affect the spectral lines and cause an empirical underestimate of the mass-loss rate.

Both stars are evolved simultaneously on the same timesteps until after the donor detaches from its Roche lobe. We follow Kolb & Ritter (1990) to calculate with an implicit scheme the mass transfer rate from optically thick layers of the donor star during RLOF. Moreover, we assume that the specific angular momentum and entropy of the transferred layers match the surface, while the chemical composition is set by the stratification of the donor star. Mass transfer is conservative until the accretor reaches critical rotation, after which rotationally-enhanced mass loss governs the mass transfer efficiency. Transferred matter which is not successfully accreted carries away the specific angular momentum corresponding to the accretor's orbital motion.

After losing their envelopes, massive donors are not expected to expand to hundreds of  $R_\odot$  during He-shell burning at the metallicity we consider (e.g., Laplace et al. 2020, however see also Gilkis et al. 2019). Thus, we stop evolving a binary system when the donor's surface He mass fraction is larger than 0.35 – indicating that a significant amount of envelope has been lost or transferred, and the radius is smaller than both the Roche radius and the terminal-age main sequence radius (TAMS, defined as when the central mass fraction of H drops below  $10^{-4}$ ). From here onwards, we continue the evolution of the accretor as a single star until its TAMS with the same setup.

We discuss some parameter variations for the physics of each star, the initial conditions, and the binary interactions in Sec. 4.

### 3. MASSIVE BINARY EVOLUTION NATURALLY EXPLAINS $\zeta$ OPHIUCHI'S PROPERTIES

We describe here the evolution of a binary system where the accretor star can broadly reproduce all the observed features of  $\zeta$  Oph. We assume initial masses  $M_1 = 25 M_\odot$ ,  $M_2 = 17 M_\odot$ , and initial period  $P = 100$  days with a metallicity of  $Z = 0.01$ .

Fig. 1 shows the Hertzsprung-Russell diagrams (HRD) of both stars. After  $\sim 7.24, the donor star (top panel) evolves off the main sequence and  $\sim 8400 later it overfills its Roche lobe (black outline of the curves). This results in a stable case B RLOF (see below). We refer to Götberg et al. (2017); Klencki et al.$$

(2020); Laplace et al. (2021); Blagorodnova et al. (2021) and references therein for a detailed description of the evolution of massive donor stars in binaries. Although our models are more massive, the qualitative behavior of the donor star is similar. Minor differences might arise because of mixing above and in the H-burning shell (e.g., Schootemeijer et al. 2019; Klencki et al. 2021), and its interplay with the mass transfer.

At the onset of RLOF, the accretor star (bottom panel of Fig. 1) is still on the main sequence with  $T_{\mathrm{eff}} \simeq 10^{4.5} \mathrm{K}$  and its central mass fraction of hydrogen is  $X(^1\mathrm{H}) \simeq 0.41$ . Because of accretion, it is pushed out of thermal equilibrium and quickly becomes over-luminous to radiate away the excess internal energy and reaches  $L \simeq 10^{5.5} L_\odot \gg L_{\mathrm{nuc}} \simeq 10^{5.1} L_\odot$ , with  $L_{\mathrm{nuc}}$  the total energy released per unit time by nuclear burning.

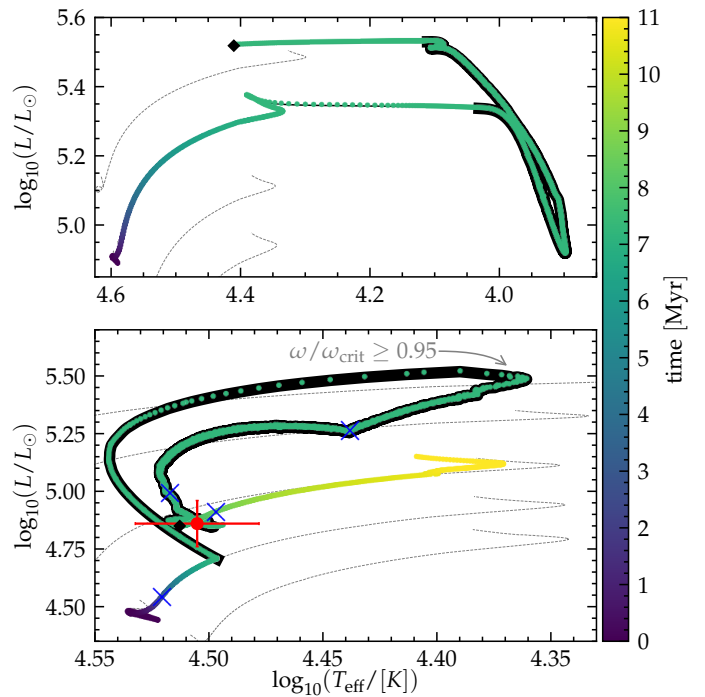


**Figure 1.** HRD for the donor star (top) and accretor star (bottom) of the progenitor binary of  $\zeta$  Oph. Each point is separated by 50 years of evolution, and the part with a black outline corresponds to the RLOF phase. The colors represent the stellar age, the red data point shows the position of  $\zeta$  Oph according to VH05, the thin blue crosses mark the position of the profiles shown in Fig. 3, and the black diamonds mark the end of the binary run. We continue the accretor evolution as a single star from there until core H depletion, hence the bottom panel shows a longer time. We emphasize the different scales on the two panels. The thin gray dashed line show the main sequence evolution of non-rotating single stars of 15, 17, 20, 25, and  $30 M_\odot$  at  $Z = 0.01$  for comparison.

The radius of the accretor increases dramatically from  $\sim 7.5 R_\odot$  to  $\sim 35 R_\odot$ , and only once the accretor reaches critical rotation (see annotation in the bottom panel of Fig. 1, roughly at the lowest  $T_{\text{eff}}$ ), the star begins contracting and its  $T_{\text{eff}}$  increases. At  $T_{\text{eff}} \simeq 10^{4.43}$  K the material transferred from the donor star becomes progressively more He-rich and CNO-processed, changing the opacity in the outer-layers of the accretor and causing a “v-shaped” feature in its evolutionary track. This indicates that the partially processed outer layers<sup>3</sup> of the donor’s core are uncovered by mass transfer. The transfer of the innermost layers of the donor puts material at high mean molecular weight  $\mu$  on top of the primordial envelope of the accretor, modifying the morphology of the evolutionary track. Because of the inverted  $\mu$  gradient, thermohaline mixing starts in the outer layers of the accreting star, and, together with rotational mixing, it progressively dilutes the surface He and N mass fractions and causes noisy features on the HR diagram (e.g., Cantiello et al. 2007). The (standard) algorithmic choices in modeling mixing and rotation might impact the morphology of the accretor’s evolutionary track during RLOF. The entire duration of RLOF is only about  $10^4$  years, and therefore unlikely to be observable to probe directly the accuracy of our treatment of mixing. We expand on the mixing processes inside the accretor in Sec. 3.1.

We evolve the binary system until the black diamonds in Fig. 1, which occurs well after the donor detaches from the Roche Lobe. At this point, the accretor is a H-rich fast-rotating star of  $\sim 20.1 M_\odot$ . Available mass estimates for the presently single  $\zeta$  Oph are highly uncertain, but most include  $20 M_\odot$  (e.g., Hoogerwerf et al. 2001, VH05, Neuhäuser et al. 2020). The accretor’s post-RLOF orbital velocity is  $v_2 \simeq 52 \text{ km s}^{-1}$ . In the subsequent evolution, wind mass loss from both stars will result in widening of the binary and slowing down the orbital motion of the accretor: we computed one binary model until the donor’s He core burning, and at that point the accretor’s orbital velocity has decreased to  $\sim 40 \text{ km s}^{-1}$ . Further decrease should be expected because of the post-He core burning wind mass loss, likely dominated by the (uncertain) mass-loss rate of the stripped donor star. Nevertheless, the value we obtain is in broad agreement with estimates of the observed runaway velocity of  $\zeta$  Oph.

Accounting for both wind mass loss and the amount of mass transferred, at the end of RLOF the donor becomes

a He star of  $\sim 9.4 M_\odot$ , likely to contract further. Depending on its wind mass-loss rate, the stripped donor’s spectrum might show only absorption lines, only emission lines, or a mixture of both (e.g., Crowther 2007; Neugent et al. 2017; Götberg et al. 2018). Its surface H mass fraction is  $\lesssim 0.2$  and the layer still containing H will possibly be removed by further wind mass loss (e.g., Götberg et al. 2017).

After the donor detaches from its Roche lobe and contracts to a radius smaller than TAMS (black diamonds in Fig. 1), we continue the evolution of the accretor as a single star with the same MESA setup until its TAMS. The main-sequence track on which the accretor settles post-RLOF has a higher luminosity compared to the original track because of the accretion of mass, and it has also a slightly steeper slope due to the close-to-critical rotation and the accretion of partially nuclearly processed material (He- and N-rich) material.

The red errorbars in the bottom panel of Fig. 1 mark the approximate position of  $\zeta$  Oph based on the spectral analysis of VH05. The color of the track in Fig. 1 indicate that our accreting star spends about  $\sim 2$  Myr within the represented errorbars after the end of RLOF. Assuming the kinematic age of  $1.78 \pm 0.21$  (Neuhäuser et al. 2020), together with the remaining lifetime of the donor of  $\sim 0.5$  Myr, our model approximately produces the correct timescale for the binary SN scenario.

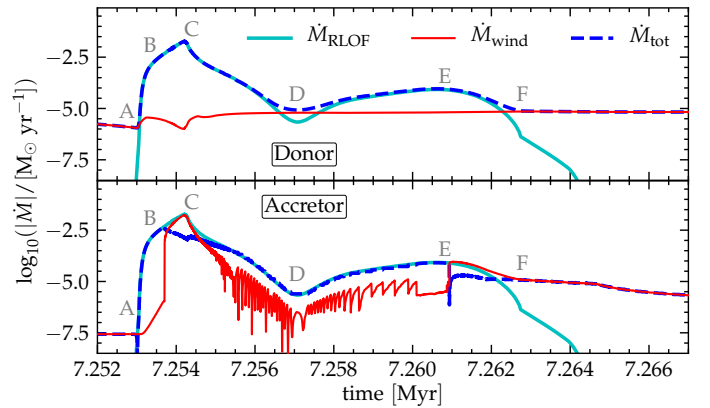


**Figure 2.** Mass transfer rates as a function of time during RLOF. The top (bottom) panel shows the donor (accretor) star. The cyan solid lines show the mass transfer rate between the two stars. The dashed blue lines show the actual change in the mass of the stars (due to the combination of wind, and accretion efficiency). The thin red lines show the wind mass loss rates. During RLOF the accretor reaches critical rotation, which leads to oscillations in the rotationally-enhanced wind mass loss.

<sup>3</sup> These are left behind by the recession in mass coordinate of the core during the donor’s main sequence.

Fig. 2 shows the rate of mass change for each star during RLOF. The top panel focuses on the donor star which loses mass via RLOF (cyan line) and winds (thin red line). The dashed blue lines show their combination resulting in the actual rate of mass change of the stars. The bottom panel shows instead the accreting star, which grows in mass because of the mass transfer. At peak, the mass transfer rates reaches very high values above  $10^{-2.5} M_{\odot} \text{ yr}^{-1}$  and taps into the optically thick matter of the donor (i.e., the donor Roche radius becomes smaller than its photosphere  $R_{\text{RL},1} < R_1$ ).

Initially, the mass transfer rate equals the mass accretion rate (bottom panel of Fig. 2), that is initially the accretion is (by construction) fully conservative. As the mass and surface rotation rate of the accretor increase, the assumed rotational-enhancement of the wind progressively increases the mass-loss rate by  $\sim 5$  orders of magnitude (Langer 1998). The rotationally-enhanced wind controls the accretion efficiency, and at  $\sim 7.254$  Myr the mass transfer becomes briefly non-conservative (where the red solid line and the cyan line overlap): the majority of the transferred mass is ejected, here we assume as a wind from the vicinity of the accretor. Consequently, the accretor slightly spins down and starts contracting (cf. Fig. 1). In the remaining evolution, the interplay between the wind mass loss rate, the spin-up due to accretion and the spin-down due to inward transport of angular momentum (see Sec. 3.2) trigger oscillations in the wind mass loss rate. Nevertheless, for most of the evolution, accretion, albeit not fully conservative, still occurs. This allows for CNO-processed material from the donor to reach the surface of the accretor during late stages of mass transfer.

At the end of RLOF, the donor star briefly expands again ( $T_{\text{eff}} \simeq 10^{4.1} \text{ K}$ ,  $L \simeq 10^{5.5} L_{\odot}$ ). This is due to the partial recombination of the now He-rich outer layers, which causes a transient surface convection layer. This causes a radial expansion of the outer convective layers and an increase in the mass-transfer rate<sup>4</sup>, despite at this point the donor is less massive than the accretor and the binary is widening. During this phase, the mass transfer becomes fully non-conservative again (in the bottom panel the wind and the mass accretion rate nearly cancel each other again at  $\sim 7.261$  Myr).

### 3.1. Mixing and composition

<sup>4</sup> With previous **MESA** releases, we found it challenging to compute our models beyond this phase: although only a very small amount of mass is involved, the onset of convection causes a large radius variation which impacts the mass transfer rate.

**MESA** treats mixing in the diffusion approximation (Paxton et al. 2011). To illustrate the dominant processes throughout the accretor’s evolution, we show in Fig. 3 the diffusion coefficients for various mixing processes as a function of mass coordinate at selected times. Each panel corresponds to one of the thin blue crosses in the bottom panel of Fig. 1, and the gray shaded areas highlight mass accreted during RLOF. The last panel roughly represents the predicted internal structure of  $\zeta$  Oph as observed today.

In Fig. 3, the thin red lines correspond to convection, with the initial convective core of  $\sim 6 M_{\odot}$  clearly visible in the first panel. In all models, a tiny sub-surface convective region is also visible in the outermost layers (see e.g., Cantiello et al. 2021). The thin blue lines show the exponentially decreasing overshooting above the convective core, which extends slightly above  $\sim 8 M_{\odot}$ . Purple and pink represent semiconvection and thermohaline mixing, respectively. Before mass transfer (left-most panel), only a small amount of sub-surface thermohaline mixing occurs, with a mass extent comparable or smaller to the sub-surface convective zone, and no semiconvection occurs. The thick cyan line corresponds to the total diffusion coefficient, obtained as the sum of the diffusion coefficients for each process modeled: where the cyan line is not overlapping with the others, rotational mixing is the dominant process.

During RLOF (second and third panel), the spin-up due to accretion causes an increase in the rotational mixing (see also Sec. 3.2). Among the rotational mixing processes we include (meridional currents, secular and dynamical shear instabilities, Goldreich-Schubert-Fricke instability), meridional currents represented by Eddington-Sweet circulations are the dominant process throughout the star. The diffusion coefficient for Eddington-Sweet circulations exceeds by about two orders of magnitude the diffusion for other processes (rotationally-driven and non). The only exception is at the core-envelope interface just outside the overshooting region, during and after RLOF. In the spun-up accretor, the evolutionary contraction of the core increases its rotational frequency and leads to the formation of a shearing layer between the core and the envelope. There, from the third panel of Fig. 3 onwards, the dynamical shear instability locally dominates producing the spike in the cyan curve (accompanied by some semiconvection in the last panel).

Late during the mass transfer (third panel), the accretion of nuclearly processed material progressively widens the thermohaline mixing region at the surface. This dominates in the outermost layers – except within the sub-surface convective zone. Thermohaline mixing



**Figure 3.** Mixing diffusion coefficients in the accretor star. From left to right, each panel shows times during the main sequence (2.71 Myr), right before the “v-shaped” feature during RLOF (7.25 Myr), close to the end of RLOF (7.26 Myr), and after mass transfer (8.38 Myr) – see the corresponding thin blue crosses in Fig. 1. The total diffusion coefficient (thick cyan line) is obtained as the sum of overshooting (thin blue line), convection (shown in red), thermohaline mixing (pink) and semiconvection (in purple), and rotational mixing – which is largely dominated by Eddington-Sweet circulations. The gray area corresponds to mass accreted during RLOF.

and Eddington-Sweet circulations together mix inwards and dilute the CNO-enriched material coming from the donor’s surface.

At the same time, the increase in the accretor mass drives rejuvenation (e.g., Schneider et al. 2016). This can be seen as a growth of the convective core from  $\sim 6 M_\odot$  to almost  $\sim 8 M_\odot$ , plus the corresponding growth of the overshooting region. This mixes inward H-rich material resulting in an elongation of the accretor’s lifetime, and at the same time mixes outward CNO-equilibrium matter, connecting the N-rich core with the outer envelope polluted from the top.

Tab. 1 summarizes the surface properties of the accretor star at the time shown in the last panel of Fig. 3, that is shortly after the RLOF phase, while the model is still roughly at the observed position of  $\zeta$  Oph. Both the mass and radius agree reasonably well with the estimates from VH05 and previous studies, that is  $20 M_\odot$  and  $8.3 \pm 1.5 R_\odot$ , respectively. Recently, optical interferometry of  $\zeta$  Oph suggested a polar radius of  $7.5 R_\odot$  and centrifugally increased equatorial radius of  $9.1 R_\odot$  (Gordon et al. 2018), also in good agreement with our model. The surface rotational velocity in excess of  $350 \text{ km s}^{-1}$  is also in the correct ballpark albeit possibly on the low

end. We discuss further rotation and angular momentum transport in Sec. 3.2.

We report the surface H mass fraction<sup>5</sup>, lower than primordial because of the accretion of nuclearly processed material, and the surface mass fraction of the most prominent species  ${}^4\text{He}$ ,  ${}^{12}\text{C}$ ,  ${}^{14}\text{N}$ ,  ${}^{16}\text{O}$ . Assuming our surface H mass fraction  $X({}^1\text{H})$ , the corresponding mass fractions of  ${}^4\text{He}$ ,  ${}^{12}\text{C}$ ,  ${}^{14}\text{N}$ ,  ${}^{16}\text{O}$  obtained by VH05 are  $0.33^{+0.14}_{-0.05}$ ,  $0.0006 \pm 0.0004$ ,  $0.002 \pm 0.001$ , and  $0.005 \pm 0.004$ . By the accretor’s TAMS, rotational mixing (and to a lesser degree thermohaline mixing) nearly homogenize the composition of the envelope of our accretor’s model. The surface mass fractions we obtain are sensitive to the interplay between several poorly understood processes treated in one dimension: mass accretion efficiency, rotationally enhanced wind mass loss, thermohaline, and inward rotational mixing. Therefore, although not perfect, we consider the match with the mass fractions reported by VH05 surprisingly satisfactory.

<sup>5</sup> We obtain the mass fractions of individual elements inverting the definition  $\varepsilon(X) = 12 + \log_{10}(N_X/N_H)$ , where  $N_X$  and  $N_H$  are the number fractions of species  $X$  and H, respectively.

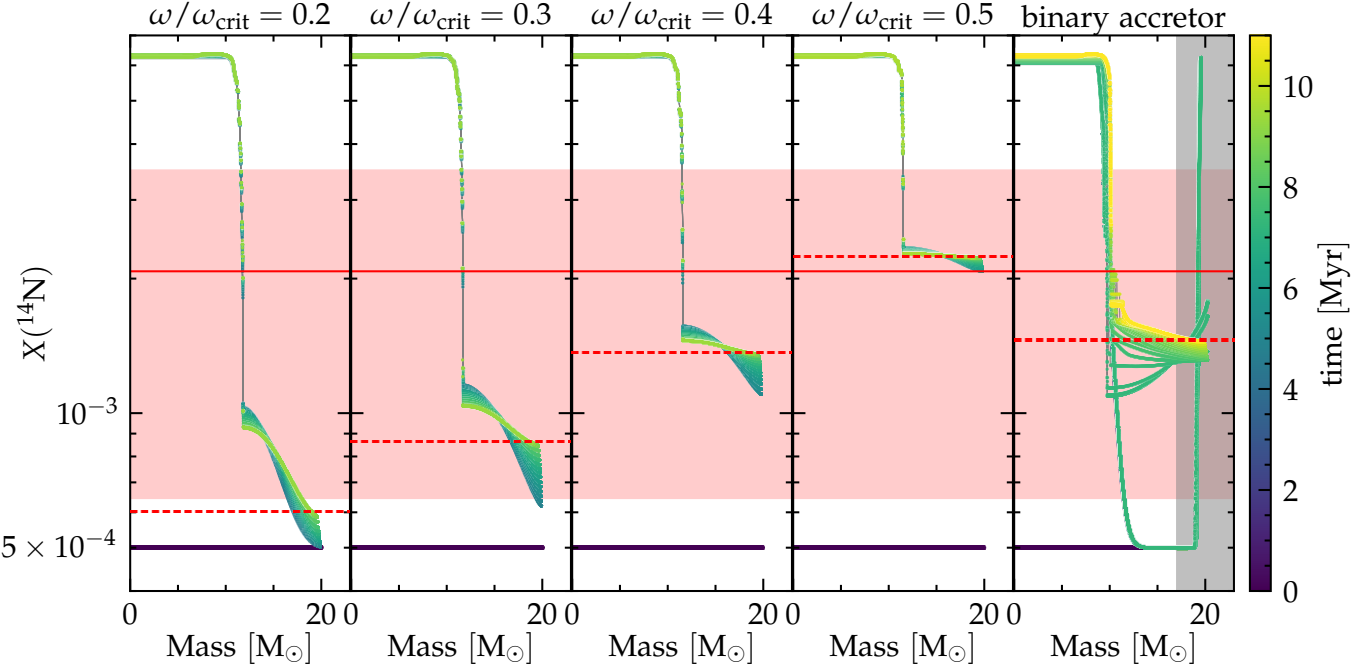


**Figure 4.**  $^{14}\text{N}$  mass fraction as a function of mass coordinate for  $20 M_{\odot}$  single star models with increasing  $\omega/\omega_{\text{crit}}$  at birth (first four panels), and for the accretor of our fiducial binary (last panel). In each panel, the darkest flat line marks the primordial value for  $Z = 0.01$ , the dashed red line marks the surface value at TAMS. In the last panel, the gray area highlights mass accreted during RLOF. The colors of each profile go from dark to light at TAMS, and selected profiles along the main sequence are shown. The solid red line and the shaded red region correspond to the mass fraction of  $^{14}\text{N}$  estimated by VH05 assuming the surface mass fraction of H from Tab. 1. The abundance of  $^{14}\text{N}$  alone is not strongly constraining. Fig. 8 shows a similar plot containing also  $^{12}\text{C}$  and  $^{16}\text{O}$ .

$M [M_{\odot}]$	$R [R_{\odot}]$	$\omega [\text{days}^{-1}]$	$v_{\text{rot}} [\text{km s}^{-1}]$	$X(^1\text{H})$	$X(^4\text{He})$	$X(^{12}\text{C})$	$X(^{14}\text{N})$	$X(^{16}\text{O})$
20.1	9.6	4.716	366.1	0.678010	0.312093	0.001344	0.001340	0.004148

**Table 1.** Properties of the accretors shortly after the end of RLOF (last thin blue cross in Fig. 1 and last panel of Fig. 3).

### 3.1.1. Comparison to single fast-rotating stars

We now compare the mixing processes happening in single rotating massive stars and in our accretor model. Fig. 4 shows the mass fraction of  $^{14}\text{N}$  as a function of mass coordinate along the evolution of three  $20 M_{\odot}$  stars initialized with  $\omega/\omega_{\text{crit}} = 0.2, 0.3, 0.4, 0.5$ . Except for the initial rotation rate and being single, these stars have the same MESA setup as our binary model. The last panel of Fig. 4 shows our accretor model. The dotted red line marks the primordial mass fraction of  $^{14}\text{N}$  for the adopted  $Z = 0.01$ , the thin dashed lines mark the surface value at TAMS.

The colored tracks show selected profiles throughout the main sequence, with lighter colors corresponding to more evolved stars. The accretor model (rightmost panel) starts as a  $17 M_{\odot}$  and is rejuvenated by binary interactions, reaching TAMS at 11.2 Myr. For comparison, the lifetime of a non-rotating single star of  $17 M_{\odot}$  is  $\sim 11.1$  Myr, while the initially  $20 M_{\odot}$  rotating models

have a main-sequence lifetime of  $\sim 9.2\text{-}9.6$  Myr (longer for higher initial rotation rates), hence their TAMS profile does not have as light a color in Fig. 4.

The first four panels of Fig. 4 show the typical rotational mixing profiles:  $^{14}\text{N}$  rapidly rises in the core because of the CNO burning, and it is then mixed outwards. At any time the  $^{14}\text{N}$  profile is monotonically decreasing in mass coordinate, and the higher the initial rotation, the higher the surface  $^{14}\text{N}$  mass fraction reached at TAMS.

Conversely, the  $^{14}\text{N}$  mass fraction profile of the accretor is *not* monotonic throughout the evolution. The profile is shaped by two main processes: (i) accretion and inward rotational (and thermohaline) mixing of CNO-processed material transferred from the inner envelope of the donor star, (ii) outward mixing of the CNO-processed material from the accretor's core caused by rotational mixing triggered by the spin-up due to accretion.

Initially, the tidally synchronized accretor star rotates too slowly ( $\lesssim 3 \text{ km s}^{-1}$ ) for significant outward rotational mixing out of the core, and until the onset of RLOF (roughly at 7.25 Myr) no appreciable variation of the surface  $^{14}\text{N}$  mass fraction occurs. During late RLOF after the “v-shaped” feature in Fig. 1, N-enriched material from the donor’s core piles onto the accretor’s surface – inside the gray area in the rightmost panel of Fig. 4. The close-to-critical rotation of the accretor and the inversion in the mean molecular weight  $\mu$  drive inward mixing of the N-rich material and dilute it in the envelope (see also Fig. 3).

Simultaneously, the mere growth in mass causes the steepening of the core-temperature gradient and increase in the convective core mass (rejuvenation, e.g., Schneider et al. 2016), driving some outward convective mixing of N-rich material. Because convection turnover timescales are much shorter than evolutionary timescales, the growth of the convective core produces “steps” at the outer edge of the core (slightly outside mass coordinate  $10 M_{\odot}$ ).

In Fig. 4, the solid red line and red shaded area across all panels show the  $^{14}\text{N}$  from VH05 (assuming the surface H mass fraction from our model listed in Tab. 1). The mass fraction of  $^{14}\text{N}$  alone is not sufficient to distinguish between these models, and already a moderate  $\omega/\omega_{\text{crit}} \geq 0.3$  is sufficient for models to reach the lower-limit of the error bar.

### 3.2. Angular momentum transport and surface rotation

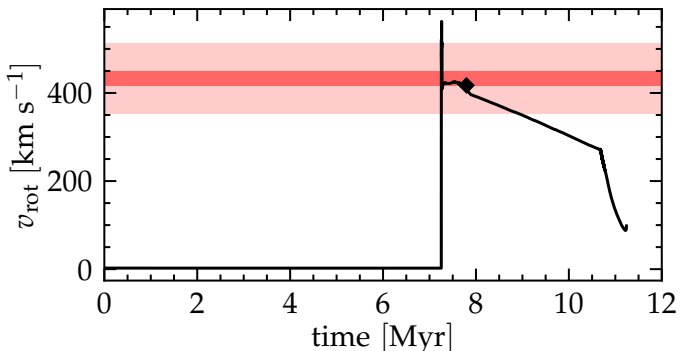


**Figure 5.** Surface averaged rotation rate for the accretor model. At  $\sim 7.25$  Myr the mass transfer quickly spins up the accretor to critical rotation. By the time the donor detaches from the RLOF the accretor is still spinning at  $\sim 400 \text{ km s}^{-1}$ . From this point (black diamond) onwards, we continue the evolution as a single star, and the accretor spins down because of wind mass loss. Note however that we use the wind mass-loss rate from Vink et al. (2001), which might be  $\sim 2$  orders of magnitude too high for  $\zeta$  Oph (Marcolino et al. 2009).

One of the main distinguishing features of  $\zeta$  Oph is its extremely high surface rotation rate. Spectroscopic measurements of the projected rotational velocity exceed  $v \sin(i) \simeq 400 \text{ km s}^{-1}$ , which implies close to critical rotation. Zehe et al. (2018) recently estimated  $v \sin(i) = 432 \pm 16 \text{ km s}^{-1}$  and  $i \sim 56$  degrees. The extremely fast rotation rate is confirmed by the centrifugal deformation found by Gordon et al. (2018).

Fig. 5 shows the surface average rotation rate of our accretor model as a function of time (ignoring the projection angle  $i$ ). The dark red band corresponds to the  $v \sin(i)$  from Zehe et al. (2018), and the lighter band shows a range of 5 times their error bar.

The initial binary is wide enough that assuming tidal synchronization at ZAMS implies a very low rotation. At 7.25 Myr, RLOF rapidly spins up the accretor to critical rotation, up to  $v_{\text{crit}} \simeq 520 \text{ km s}^{-1}$  (averaged over the surface of the star). The star remains fast rotating throughout the mass transfer phase, which ends at the black diamond in Fig. 5. In the remaining evolution, the star spins down progressively through wind mass loss, and within  $\sim 2$  Myr its averaged surface rotational velocity drops below  $350 \text{ km s}^{-1}$ . Close to the end of the main sequence, the increase in wind mass loss rate and internal transport of angular momentum causes a change in the spin-down slope. This effect is also seen in the late main-sequence evolution of single stars rotating rapidly from ZAMS.

Fig. 5 shows that, without accounting for the inclination angle, our model can retain a significant surface rotation for a time comparable to the kinematic age of the star, which is shorter than the remaining main-sequence lifetime. We emphasize that throughout its evolution this model is computed using the Vink et al. (2000, 2001) wind mass-loss rate with full efficiency. This is two orders of magnitude higher than the wind mass loss rate reported by Marcolino et al. (2009) (weak wind problem), however, see also Lucy 2012; Lagae et al. 2021. While this may impact the evolution of the binary even before RLOF, it increases the spin-down rate of our model compared to the observations. We expect that an accreting star modeled with lower wind-mass loss rate post-RLOF would retain an even higher surface rotation for longer (see also Sec. 4.1).

#### 3.2.1. Comparison to single fast-rotating stars

To illustrate the angular momentum transport in our accretor stars, it is helpful to compare with the single rotating  $20 M_{\odot}$  models. Typically, single stars are assumed to be solid-body rotators at ZAMS. Their internal rotational profile evolves differently than the profile

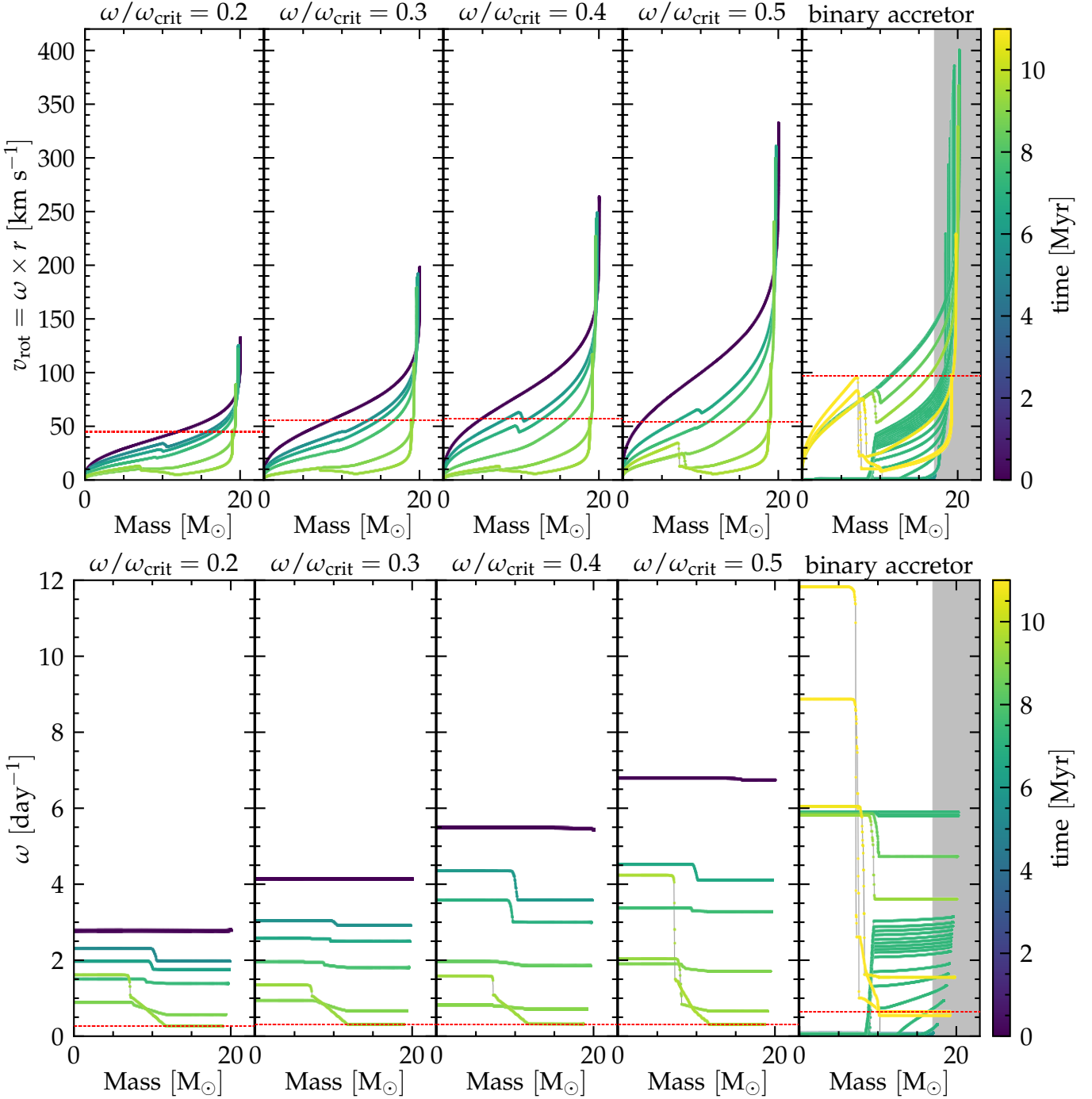


**Figure 6.** Top: Internal rotational profile for  $20 M_{\odot}$  single star models with increasing  $\omega/\omega_{\text{crit}}$  at birth (first four panels), and for the accretor of our fiducial binary. Bottom: internal rotational frequency profile. As in Fig. 4, the colors go from dark (close to ZAMS) to light at TAMS. In the top panel the thin dashed red line mark the TAMS surface rotation rate. In the rightmost panel, the gray area indicates mass accreted during RLOF. The yellow lines (TAMS) in the last panel show that the core of the accretor is rotating almost as fast as its surface despite its much smaller radius, and both are faster than the surface of single star models.

obtained spinning up the secondary star at a later evolutionary stage, from its surface, and to critical rotation.

The top row of Fig. 6 shows the internal rotational velocity  $v_{\text{rot}} = \omega \times r$ , while the bottom row shows the  $\omega$  profile. As in Fig. 4, the first four panels in each row show single rotating stars with increasing initial  $\omega/\omega_{\text{crit}}$ , the last panels shows our accretor model, and the colors go from dark (close to ZAMS) to light (TAMS). Because of rejuvenation, the accretor has a longer main-sequence life-time compared to a star of the same final mass, hence the lighter colors in the last panels (see Sec. 3.1.1). The gray area in the rightmost panels highlights matter accreted during RLOF.

The thin dashed red lines in each panel of the top row of Fig. 6 mark the TAMS surface rotation rates: all our single star models reach a TAMS surface  $v_{\text{rot}} \simeq 50 - 60 \text{ km s}^{-1}$ . Initially faster rotating models spin down more in their outer layers, have slightly longer main sequence lifetimes (because of rotational mixing increasing the available fuel), and develop stronger differential rotation. As the core contracts and spins up, the single star profiles show the progressive development of a core-envelope interface.

Conversely, the last panel shows that the entire interior of the accretor has a negligible rotational velocity until RLOF (starting at 7.25 Myr). Because of binary interactions, the accretor is spun up late in its evolution, up to critical rotation  $\omega/\omega_{\text{crit}} \simeq 1$ , and from the surface. In our model, inward transport of angular momentum creates a  $v_{\text{rot}}$  profile monotonically increasing from the center to the surface (green lines of the last panel in the top row). Late during mass transfer, the accretor achieves rigid and close to critical rotation (flat profiles in the last panel on the bottom row of Fig. 6). After the end of RLOF, the accretors envelope spins down because of winds. By the end of the main-sequence evolution of the accretor, the surface still spins with  $v_{\text{rot}} \simeq 100 \text{ km s}^{-1}$  (twice as fast as the single star models).

Perhaps more importantly, the outer-edge of the core has a similar rotational velocity as the surface, and much larger than the rotational velocity of the single star models. This is because the evolutionary contraction (decrease in  $r$ ) of the core results in a significant increase of  $\omega$  to conserve the angular momentum that cannot be transferred to the outer layers. The core-envelope interface of the accretor at TAMS is much more prominent than in single rotating stars. The faster core rotation of binary accretors spun up late and up to critical rotation might have important implications for the explosion of the initially less massive star of a binary, the spin of the resulting compact objects, and the analy-

sis of gravitational-wave events (e.g., Zaldarriaga et al. 2018; Qin et al. 2018; Callister et al. 2020).

#### 4. ROBUSTNESS OF THE MODELS AND DISCUSSION

Models of the interior evolution of stars require the choice of several poorly constrained parameters, the majority arising from the one-dimensional representation of multi-dimensional phenomena (convection, mixing, rotation, etc.). This remains true when modeling two stars in a binary, with the added caveat that an even larger number of parameters enter in the treatment of binary interactions (and in particular mass transfer). This emphasizes the need for observational constraints and motivated us to compare our models to the well characterized  $\zeta$  Oph.

Accretor stars are expected in most populations of (massive) stars, both in clusters (e.g., Chen & Han 2009; Wang et al. 2020) and in the field (e.g., de Mink et al. 2011, 2013). However, these might not obviously stand out as binary products (e.g., Renzo et al. 2019). Therefore, to inform the search for accretor stars in observed samples, it is also necessary to characterize the robustness of model predictions against numerical, physical, and algorithmic choices.

In Sec. 4.1 we report on exploration of parameter variations for each individual star in the binary. We discuss parameters governing the mass transfer phase in Sec. 4.2, the initial binary architecture in Sec. 4.3, and the consequences of the assumed SN explosion of the companion in Sec. 4.4.

##### 4.1. Uncertainties in the single-star physics

For our model of Sec. 3, we have assumed an initial metallicity  $Z = 0.01$  informed by the asteroseismology of low mass stars in the parent association Upper-Centaurus-Lupus (e.g., Murphy et al. 2021). Moreover, we have assumed that mass fractions of each element scale with the Solar values (Grevesse & Sauval 1998), which might not be appropriate especially for massive stars (e.g., Grasha et al. 2021). With these assumptions, the initial mass fraction of  $^{12}\text{C}$  and  $^{14}\text{N}$  are lower than the observed values for  $\zeta$  Oph. Even though their values at the surface of the accretor increase during mass transfer, our model still slightly under-predicts them. Improved agreement could be obtained changing the ratio of abundances to non-solar values, or by changing the efficiency of downward rotational and thermohaline mixing which dilutes the accreted material into the secondary's envelope.

We also run a model identical to the one described in Sec. 3, except with  $Z = Z_{\odot} = 0.0142$  (Asplund

et al. 2009). Qualitatively, the binary evolution remains similar, with the higher metallicity stars having slightly larger radii and cooler  $T_{\text{eff}}$  at a given luminosity. This still produces a stable case B RLOF, however, the accretor track is displaced on the right on the HRD. Thus, matching the high present-day  $T_{\text{eff}} = 32\,000 \pm 2\,000$  of  $\zeta$  Oph (e.g., VH05) requires more massive and hotter accretors (see also Sec. 4.3).

Rotation is a critical ingredient of our models: it governs the equatorial radius and thus  $\omega/\omega_{\text{crit}}$  and mass transfer efficiency (see Sec. 4.2), through Eddington-Sweet meridional circulations it determines outward mixing from the core, and more importantly inward mixing from the surface. We emphasize that the shellular approximation used in one-dimensional stellar evolution codes might not be appropriate for  $\omega/\omega_{\text{crit}} \simeq 1$  reached by our accretor star during RLOF. Decreasing by a factor of 10 the diffusion coefficient for Eddington-Sweet meridional circulations has a very small effect on the HRD evolution of the accretor. However, the noisiness during the late RLOF phase (for  $T_{\text{eff}} \gtrsim 10^{4.5}$  K in Fig. 1) increases in amplitude slightly, confirming that the details of this part of the evolution are sensitive to the treatment of rotational mixing. We were unable to run models turning completely off Eddington-Sweet meridional circulations past the “v-shaped” feature in Fig. 1.

Our models assume a Spruit-Tayler dynamo (Spruit 2002) for the transport of angular momentum throughout the evolution. Adopting the stronger angular momentum transport from Fuller et al. (2019) might result in a more efficient spin-down of the surface during RLOF, possibly allowing for more accretion of mass.

The accretor is spun up late, from the surface inwards, and to critical rotation compared to single star models which are initialized at ZAMS with rigid rotation. Late during the mass transfer, even the weaker core-envelope coupling of Spruit (2002) is sufficient for the accretor to achieve rigid rotation. Subsequently, the envelope spins down because of wind mass loss and more importantly the core spins significantly up because of its evolutionary contraction. We expect that following Fuller et al. (2019) the core would lose more angular momentum to the envelope, decreasing its rotational velocity. Nevertheless, we expect that the difference with single star rotational profiles would remain because of the shorter evolutionary time left.

During RLOF, thermohaline mixing in the envelope also becomes important. We have explored models enhancing the efficiency of this mixing process by a factor of 100 (Schootemeijer et al. 2019), however, this caused our models to crash during RLOF after the “v-shaped”

feature corresponding to the accretion of nuclearly processed material.

Finally, to address the “weak wind problem”, we also attempted running models with artificially decreased wind mass loss rate (e.g., Renzo et al. 2017), but these resulted in super-critical  $\omega/\omega_{\text{crit}} > 1$  accretor stars with untrustworthy numerical results.

While the number of free parameters resulting in a successful computation is rather limited, we emphasize that this remains often true for calculation of single massive star evolution.

#### 4.2. Uncertainties in the treatment of mass transfer

We regulate the accretion efficiency through the rotational enhancement of mass loss (e.g., Langer 1998). However, whether critical rotation can effectively stop the accretion of matter is unclear. Popham & Narayan (1991) and Paczynski (1991) argued that accretion of mass (but no angular momentum) might be possible even at or beyond critical rotation.

During RLOF, the total amount of mass lost by the donor is  $\Delta M_{\text{donor}} \simeq 10.6 M_{\odot}$ , of which only  $\Delta M_{\text{accretor}} \simeq 3.4 M_{\odot}$  are successfully accreted. This corresponds to an overall mass transfer efficiency  $\beta_{\text{RLOF}} \equiv |\Delta M_{\text{accretor}}|/|\Delta M_{\text{donor}}| \simeq 0.32$ , although the accretion efficiency is *not* constant throughout the mass transfer (e.g., van Rensbergen et al. 2006). In our models, the mass transfer efficiency depends on the radial and rotational evolution of the accreting star. During RLOF, the accretor is out of gravothermal equilibrium with significant impact on its radius and ultimately on the amount of mass transferred and its angular momentum. In reality, the gas stream between the two stars, the formation of a disk, and the geometric distortion of the outer layers because of the centrifugal forces would not follow the spherical symmetry imposed by 1D codes such as MESA.

While the mass transfer efficiency  $\beta_{\text{RLOF}}$  and importantly its time-evolution need further attention, we emphasize that most studies, especially using rapid population synthesis tools, typically assume a constant  $\beta_{\text{RLOF}}$  and neglect to model the out-of-equilibrium phase of the accretor and how this can impact the binary and orbital evolution.

Another free parameter in the treatment of mass transfer is the specific angular momentum of the accreted material. In our models, for the sake of numerical stability, we assume the incoming material and the stellar surface to have the same specific angular momentum. This approximation corresponds to a scenario where angular momentum transport in the circumstellar disk during RLOF quickly homogenizes the rotation

rate and provides a relatively slow spin-up of the accretor star.

We also attempted calculations using the algorithm from de Mink et al. (2013) based on the fit from Ulrich & Burger (1976) to the numerical results of Lubow & Shu (1975). This algorithm distinguishes between direct impact of the L1 stream and circumstellar disk formation and determines the specific angular momentum of the incoming material. However, these models proved numerically more unstable and providing less trustworthy results. Generally speaking, allowing for a faster accretion of angular momentum results in less radial expansion of the accretor (cf. Fig. 1), faster spin-up, and a lower overall mass transfer efficiency  $\beta_{\text{RLOF}}$ .

Finally, while the composition of the transferred material is determined by the structure of the donor and the mass transfer rate calculated following Kolb & Ritter (1990), we still need to specify its specific entropy when it reaches the accretor surface. We follow the common practice of assuming the specific entropy of the incoming material to be same as the accreting surface. The scenario justifying this hypothesis is that during RLOF the matter is sufficiently optically thin so radiative processes can rapidly equalize the entropy between the RLOF stream and the accreting surface. However, the very large mass-transfer rates we find (cf. Fig. 2) might result in optically thick flows for which this approximation might not be appropriate.

### 4.3. Variations in initial binary parameters

The initial donor mass  $M_1$ , mass ratio  $q = M_2/M_1$ , and the period of the progenitor binary of  $\zeta$  Oph cannot be directly constrained from observations. We have explored variation in these values, and the qualitative behavior of the models is similar.

Shorter initial periods results in larger post-RLOF orbital velocities, and thus larger runaway velocities if the binary is disrupted at the first SN (see Sec. 4.4). For example, taking  $P=75$  days (cf. 100 days in our fiducial model in Sec. 3), the binary still experiences stable case B mass transfer, but the post-RLOF orbital velocity of the accretor is about  $60 \text{ km s}^{-1}$ , that is  $\sim 10 \text{ km s}^{-1}$  higher than in our fiducial model.

Increasing the donor mass also has a similar effect on the post-RLOF orbital velocity of the accretor. Using  $M_1 = 30 M_\odot$  (cf.  $25 M_\odot$  in Sec. 3),  $M_2 = 17 M_\odot$ , and  $P=100$  days, we obtain a post-RLOF velocity of  $65 \text{ km s}^{-1}$ . However, this produces a stripped donor of  $\sim 16 M_\odot$  at RLOF detachment, with stronger wind mass loss. Therefore this binary is expected to widen relatively more than our fiducial model of Sec. 3, slowing down the secondary. The increased mass of the stripped

star could also imply a lower chance of exploding for the donor (however, see Sec. 4.4).

The higher  $M_1$  does not significantly change the post-RLOF total mass of the accretor, with  $M_2$  remaining about  $\sim 20.5 M_\odot$ , since in our models accretion is regulated mostly by the spin up of the accretor, and we do not couple the specific angular momentum of the transferred material to the orbit or the donor's spin.

However, changing the initial mass ratio also changes the difference between the main-sequence lifetime of the two stars, and thus how far along the main sequence the accretor is at the onset of RLOF. The observed position of  $\zeta$  Oph on the HRD, particularly its relatively high  $T_{\text{eff}}$  are difficult to reproduce assuming initially less massive accretors (which would remain too cool even after accreting mass), or more equal initial mass ratio (which would produce a too evolved accretor at the onset of mass transfer).

### 4.4. The explosion of the former companion

Throughout this study, we have assumed the “binary SN scenario” to explain the runaway nature of  $\zeta$  Oph: after the mass transfer phase, the explosion of the donor breaks the binary and ejects the accretor at roughly its pre-explosion orbital velocity (e.g., Renzo et al. 2019). This fate occurs to the majority of massive binary systems, and  $\zeta$  Oph might be the best example of it (e.g., Blaauw 1952, 1961; Hoogerwerf et al. 2000). Neuhäuser et al. (2020) suggested not only the companion successfully exploded producing the pulsar PSR B1706-16, but that the explosion produced radioactive  $^{60}\text{Fe}$  which polluted Earth.

From kinematic and orbital considerations they estimated the pulsar received a natal kick of  $253 \pm 54 \text{ km s}^{-1}$ , which would be sufficiently large to unbind the binary (Kalogera 1996; Tauris 2015). The ejecta mass would depend on the post-RLOF wind mass loss of our donor star, which we do not model. At the end of our binary model (black diamond in Fig. 1), our stripped donor is  $\sim 9.4 M_\odot$ , with a surface H fraction of  $X \lesssim 0.2$  for a layer of  $\Delta M \simeq 2.5 M_\odot$ . Its wind mass-loss rate is  $\sim 10^{-5} M_\odot \text{ yr}^{-1}$  (cf. Fig. 2), likely to increase as it contracts into a Wolf-Rayet star and increases its luminosity and effective temperature. We expect its explosion to appear as H-less type Ib SN. Although our stripped donor is rather massive, recent studies hints at a higher “explodability” of donor stars in binary systems (e.g., Schneider et al. 2021; Laplace et al. 2021; Vartanyan et al. 2021).

We have neglected the impact of the explosion on the structure of the accretor star. At the time of the explosion, the accretor subtends a solid angle  $\sim R^2/a^2 \simeq$

0.05 degrees with  $R$  the accretor radius and  $a$  the binary separation. We neglect the post-RLOF wind-driven orbital widening for this estimate. The blast wave will hit the accretor causing mass loss – directly via ablation and by injecting energy in the envelope, inflating it and enhancing its wind (Wheeler et al. 1975; Tauris & Takens 1998; Podsiadlowski 2003; Hirai et al. 2018). Because of the SN shock, the just ejected new runaway star might appear bloated and redder (long before it overtakes the slowing SN remnant). The impact of this brief out of thermal equilibrium phase on the stellar spin should be investigated further.

Using 2D hydrodynamic simulations of the star-SN ejecta interactions in close binaries ( $a \lesssim 60 R_\odot$ , cf.  $a \gtrsim 343 R_\odot$  in our fiducial binary model), Hirai et al. (2018) found that the companion star recovers its pre-explosion luminosity and effective temperature within a few years to decades, and the amount of mass removed by the SN shock is  $\lesssim 10^{-2} M_\odot$ . The SN ejecta might also pollute the surface of the runaway depositing processed nuclear material (e.g., Przybilla et al. 2008; Suda et al. 2021). However, for the large final separation of our model, little pollution is expected and enhanced mass loss and inward mixing might quickly dilute any signature below detectable levels.

## 5. CONCLUSIONS

We presented self-consistent spherically-symmetric MESA calculations of a binary system where both stars are evolved simultaneously and coupled. As a first application, we focused on finding a model for  $\zeta$  Oph, assuming its runaway nature is explained by the binary SN scenario.

We found that it is possible to explain the observed features of  $\zeta$  Oph with a relatively wide and massive binary initialized with  $M_1 = 25 M_\odot$ ,  $M_2 = 17 M_\odot$ , and  $P = 100$  days at metallicity  $Z = 0.01$  (see Sec. 3). This binary system experiences dynamically-stable Roche lobe overflow after the end of the main sequence of the initially more massive star (case B). Standard stellar physics assumptions for modeling rotation, mixing, and mass transfer in binaries (see Sec. 2 and Appendix A) reproduce reasonably well the main features of  $\zeta$  Oph. Specifically,  $\sim 1.5 - 2$  Myrs after the end of mass transfer, corresponding to the remaining donor’s lifetime at the end of our simulations plus the kinematic age of  $\zeta$  Oph, the accretor star in our model has the following quantities in the correct ballpark:

- Luminosity and effective temperature;
- Total mass;
- Runaway space velocity;

- Fast surface rotation (albeit possibly on the low side, cf. weak wind problem);
- enhanced  $^4\text{He}$  and  $^{14}\text{N}$  surface mass fraction;
- small variations in  $^{12}\text{C}$  and  $^{16}\text{O}$  surface mass fractions.

We emphasize that the surface composition alone would not be a smoking-gun, especially given the large uncertainties in the treatment of rotation and mixing in stellar evolution models. However, alternative scenarios where  $\zeta$  Oph evolved as a single fast-rotating star require ad-hoc explanations for the runaway velocity, and have been shown by VH05 to struggle in reproducing surface mass fractions, apparent age, mass, and rotation rate simultaneously.

In contrast with van Rensbergen et al. (1996), in our model the  $^{14}\text{N}$ - and  $^4\text{He}$ -rich surface composition is not the result of pure outward rotational mixing. Instead, this material is transferred from the receding core of the donor star and mixed from the surface inwards by rotation and, to a smaller degree, by thermohaline mixing. Thus, the present day surface mass fractions of  $\zeta$  Oph put a coupled constraint on the mass transfer efficiency and mixing in the accretor. Therefore, such star should *not* be used to calibrate models of rotational mixing in single star evolution, nor its more extreme version of chemically homogeneous evolution.

The spin up of the accreting star occurs late in its evolution ( $t \gtrsim 7.25$  Myr for our fiducial binary) and reaches to critical surface rotation  $\omega/\omega_{\text{crit}} \simeq 1$ . The treatment of close-to-critical rotation impacts the accretion efficiency, the radius evolution, and the inward mixing.

An important difference we find between our accretor model and comparable fast-rotating single star models is their internal rotation profile. Single-stars rotating rapidly from birth are initialized as rigid rotators, and spin down significantly both at the surface and inside. Conversely, in our accretor models angular momentum is injected late and from the top. When this angular momentum is transported into the core by the Spruit-Tayler dynamo, it results in a much faster rotating helium core, with potential implications for the final explosion and the resulting compact object born from the accretor star in an interacting binary system.

We also consider variations in the initial parameters and in the implementation of physical processes, discussed in Sec. 4. Less massive accretors remain too cool throughout the evolution to be compatible with  $\zeta$  Oph, and more equal initial mass ratios lead to a more evolved accretor at the onset of mass-transfer, again resulting in too cool temperatures. Increasing the donor’s initial

mass might result in stripped stars unlikely to form a neutron star in their final SN explosion.

Improving our understanding of the evolution of the initially less massive stars in massive binary systems is crucial for the upcoming large surveys (astrometric, photometric, spectroscopic, and in time domain) and for the understanding of the evolution of gravitational-wave progenitors in isolated binaries. Although presently single, the nearest O-type star to Earth,  $\zeta$  Oph, can be used as an anchor point for the modeling of accretors. Our models demonstrate that a broad agreement with observations can be achieved with standard stellar evolution assumptions. Future efforts should extend these models to a wider mass, period, mass ratio, and metallicity range to investigate the impact of binary evolution on

the life, explosion, and after-life of the secondary stars in massive binary systems.

*Software:* MESA (Paxton et al. 2011, 2013, 2015, 2018, 2019), mesaSDK (Townsend 2018), ipython/jupyter (Pérez & Granger 2007), matplotlib (Hunter 2007), mesaPlot (Farmer 2018), NumPy (van der Walt et al. 2011).

## ACKNOWLEDGMENTS

We are grateful to E. Zapartas, A. Jermyn, M. Cantiello, and R. Neuhäuser for helpful discussions.

## APPENDIX

### A. MESA SETUP

We use MESA version 15140 to compute our models. The MESA equation of state (EOS) is a blend of the OPAL Rogers & Nayfonov (2002), SCVH Saumon et al. (1995), PTEH Pols et al. (1995), HELM Timmes & Swesty (2000), and PC Potekhin & Chabrier (2010) EOSes.

OPAL (Iglesias & Rogers 1993, 1996) provides the main radiative opacities, with low-temperature data from Ferguson et al. (2005) and the high-temperature from Buchler & Yueh (1976). Electron conduction opacities are from Cassisi et al. (2007).

Nuclear reaction rates are a combination of rates from NACRE (Angulo et al. 1999), JINA REACLIB (Cyburt et al. 2010), plus additional tabulated weak reaction rates Fuller et al. (1985); Oda et al. (1994); Langanke & Martínez-Pinedo (2000). Screening is included via the prescription of Chugunov et al. (2007). Thermal neutrino loss rates are from Itoh et al. (1996). We use a 22-isotope nuclear network (approx\_21\_plus\_cr56).

The inlists, processing scripts, and model output will be made available at [10.5281/zenodo.4701565](https://doi.org/10.5281/zenodo.4701565).

### B. RESOLUTION TESTS

We extensively check the numerical convergence of our stellar evolution calculations with increasing number of mesh points. Fig. 7 shows that all the features described extensively here do not vary when increasing the spatial resolution by decreasing `mesh_delta_coeff`. The right panel shows the number of mesh points for the accretor (top) and donor (bottom) as a function of the model number (akin to an arbitrary time coordinate). About  $\sim 7000$  MESA models are used to compute the binary evolution. The higher resolution run has  $\sim 20\%$  more mesh

points. The left panel shows the HRD evolution until the detachment of the binary for the two accretor models (pink/red) and the two donor models (blue/cyan).

Similarly, we tested the numerical convergence with decreasing timestep size. This can be done decreasing the parameter `mesh_time_coeff`. However, we were unable to successfully compute models at higher temporal resolution. Partial results show a good agreement with our fiducial model until MESA becomes unable to find a satisfying numerical solution to the stellar structure equations (typically during RLOF). Lower temporal resolution models showed a similar qualitative agreement but increased noisiness during the late RLOF phase. For our fiducial model the adaptive timestep size never exceeds  $10^{3.8}$  years with typical pre-RLOF timesteps of the order of  $10^{3.2}$  years and sub-decade during RLOF. The main factor limiting the timestep sizes is the change of surface angular momentum in both stars during the mass transfer.

### C. INTERNAL COMPOSITION PROFILE EVOLUTION

Fig. 8 compares the internal evolution of the composition profile of single rotating stars with our accretor model. We show mass fractions of  $^{12}\text{C}$  and  $^{16}\text{O}$  to complement the mass fraction of  $^{14}\text{N}$  shown in Fig. 4, and reproduced also in the middle panel of Fig. 8.

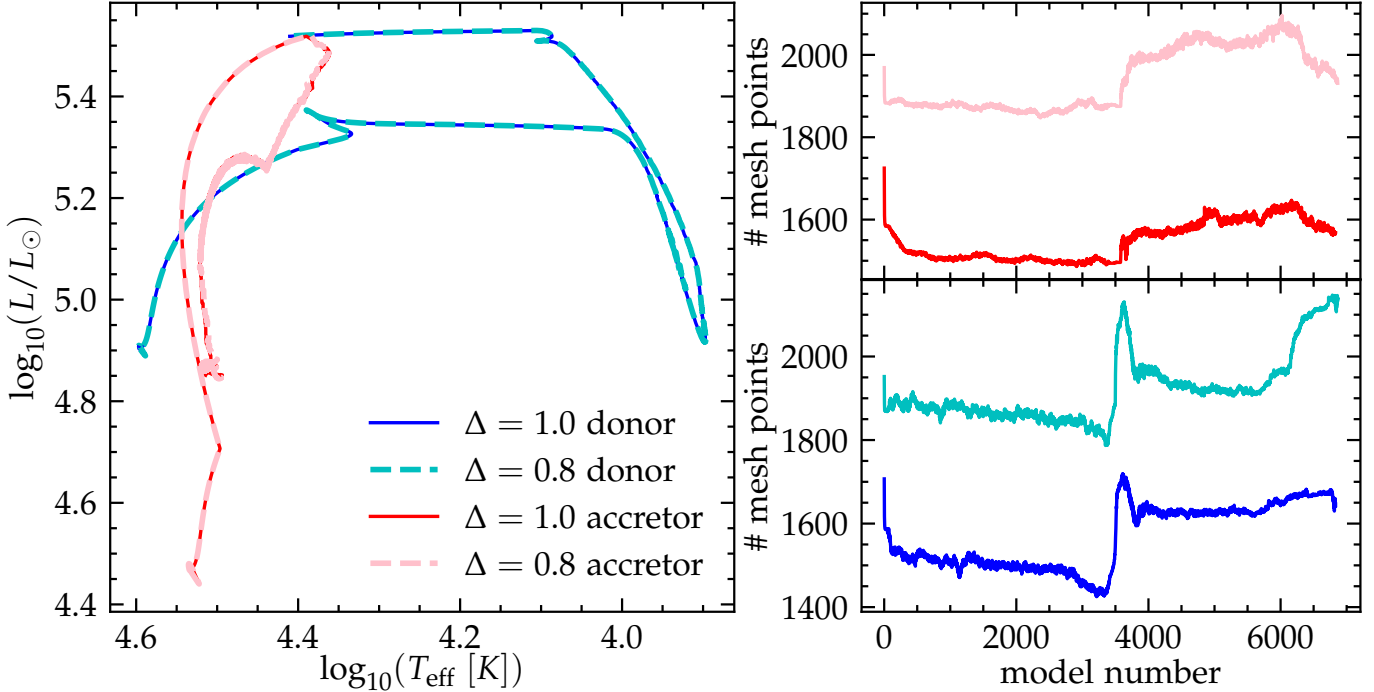


**Figure 7.** Left: HRD comparison for our fiducial binary model varying the number of mesh points. We only show the evolution until our definition of RLOF detachment. Right: number of mesh points as a function of timestep number. In both panels, the blue/cyan tracks show the donor stars, the red/pink tracks show the accretor. Thicker dashed lines correspond to the models at higher resolution (i.e., lower  $\Delta$  which indicates the value of `mesh_delta_coeff`).

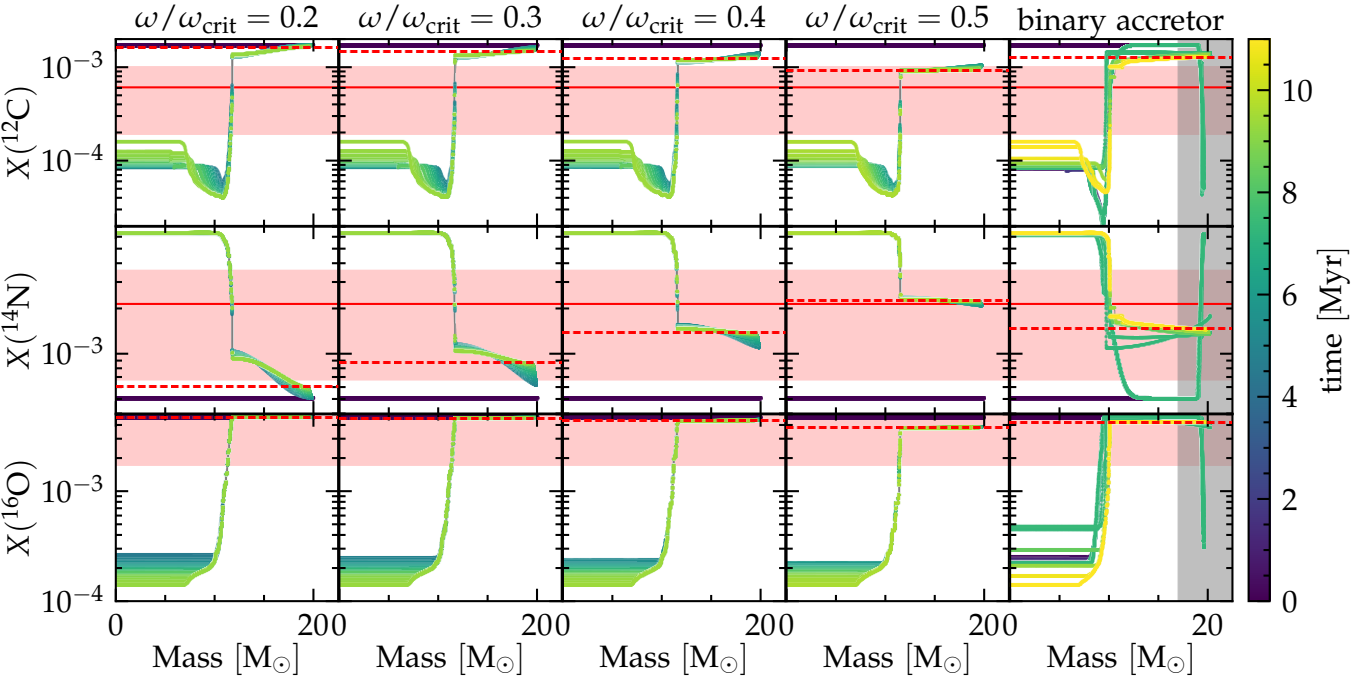


**Figure 8.** Same as Fig. 4, but for  $^{12}\text{C}$  (top panel), and  $^{16}\text{O}$  (bottom panel). The first four panels show single rotating stars of initially  $20 M_\odot$ , the rightmost panel shows the accretor in our fiducial binary. The middle panel is exactly the same as Fig. 4. Thick red dotted lines mark the initial mass fractions, thin red dashed lines the TAMS surface mass fraction, the solid red lines and the semi-transparent red bands correspond to the values inferred by VH05 using the surface H mass fraction from our model. The tracks go from dark (roughly corresponding to ZAMS) to light colors, with the lightest color corresponds to TAMS.

## REFERENCES

- Almeida, L. A., Sana, H., Taylor, W., et al. 2017, *A&A*, 598, A84, doi: [10.1051/0004-6361/201629844](https://doi.org/10.1051/0004-6361/201629844)
- Angulo, C., Arnould, M., Rayet, M., et al. 1999, *Nuclear Physics A*, 656, 3, doi: [10.1016/S0375-9474\(99\)00030-5](https://doi.org/10.1016/S0375-9474(99)00030-5)
- Asplund, M., Grevesse, N., Sauval, A. J., & Scott, P. 2009, *ARA&A*, 47, 481, doi: [10.1146/annurev.astro.46.060407.145222](https://doi.org/10.1146/annurev.astro.46.060407.145222)
- Belczynski, K., Holz, D. E., Bulik, T., & O'Shaughnessy, R. 2016, *Nature*, 534, 512, doi: [10.1038/nature18322](https://doi.org/10.1038/nature18322)
- Blaauw, A. 1952, *BAN*, 11, 414  
—. 1961, *BAN*, 15, 265
- Blaauw, A. 1993, in *Astronomical Society of the Pacific Conference Series*, Vol. 35, Massive Stars: Their Lives in the Interstellar Medium, ed. J. P. Cassinelli & E. B. Churchwell, 207
- Blagorodnova, N., Klencki, J., Pejcha, O., et al. 2021, arXiv e-prints, arXiv:2102.05662.  
<https://arxiv.org/abs/2102.05662>
- Bodensteiner, J., Baade, D., Greiner, J., & Langer, N. 2018, *A&A*, 618, A110, doi: [10.1051/0004-6361/201832722](https://doi.org/10.1051/0004-6361/201832722)
- Bodensteiner, J., Shenar, T., & Sana, H. 2020, *A&A*, 641, A42, doi: [10.1051/0004-6361/202037640](https://doi.org/10.1051/0004-6361/202037640)
- Boubert, D., & Evans, N. W. 2018.  
<https://arxiv.org/abs/1804.05849>
- Braun, H., & Langer, N. 1995, *A&A*, 297, 483
- Broekgaarden, F. S., Berger, E., Neijssel, C. J., et al. 2021, arXiv e-prints, arXiv:2103.02608.  
<https://arxiv.org/abs/2103.02608>
- Brott, I., de Mink, S. E., Cantiello, M., et al. 2011, *A&A*, 530, A115, doi: [10.1051/0004-6361/201016113](https://doi.org/10.1051/0004-6361/201016113)
- Buchler, J. R., & Yueh, W. R. 1976, *ApJ*, 210, 440, doi: [10.1086/154847](https://doi.org/10.1086/154847)
- Callister, T. A., Farr, W. M., & Renzo, M. 2020, arXiv e-prints, arXiv:2011.09570.  
<https://arxiv.org/abs/2011.09570>
- Cantiello, M., Lecoanet, D., Jermyn, A. S., & Grassitelli, L. 2021, arXiv e-prints, arXiv:2102.05670.  
<https://arxiv.org/abs/2102.05670>
- Cantiello, M., Yoon, S., Langer, N., & Livio, M. 2007, *A&A*, 465, L29
- Cassisi, S., Potekhin, A. Y., Pietrinferni, A., Catelan, M., & Salaris, M. 2007, *ApJ*, 661, 1094, doi: [10.1086/516819](https://doi.org/10.1086/516819)
- Chen, X., & Han, Z. 2009, *MNRAS*, 395, 1822, doi: [10.1111/j.1365-2966.2009.14669.x](https://doi.org/10.1111/j.1365-2966.2009.14669.x)  
—. 2010, *Ap&SS*, 329, 277, doi: [10.1007/s10509-010-0368-0](https://doi.org/10.1007/s10509-010-0368-0)
- Chugunov, A. I., Dewitt, H. E., & Yakovlev, D. G. 2007, *PhRvD*, 76, 025028, doi: [10.1103/PhysRevD.76.025028](https://doi.org/10.1103/PhysRevD.76.025028)
- Claret, A., & Torres, G. 2017, *ApJ*, 849, 18, doi: [10.3847/1538-4357/aa8770](https://doi.org/10.3847/1538-4357/aa8770)
- Crowther, P. A. 2007, *ARA&A*, 45, 177, doi: [10.1146/annurev.astro.45.051806.110615](https://doi.org/10.1146/annurev.astro.45.051806.110615)
- Cyburt, R. H., Amthor, A. M., Ferguson, R., et al. 2010, *ApJS*, 189, 240, doi: [10.1088/0067-0049/189/1/240](https://doi.org/10.1088/0067-0049/189/1/240)
- De Donder, E., Vanbeveren, D., & van Bever, J. 1997, *A&A*, 318, 812
- de Jager, C., Nieuwenhuijzen, H., & van der Hucht, K. A. 1988, *A&AS*, 72, 259
- de Mink, S. E., Langer, N., & Izzard, R. G. 2011, *Bulletin de la Societe Royale des Sciences de Liege*, 80, 543.  
<https://arxiv.org/abs/1010.2200>
- de Mink, S. E., Langer, N., Izzard, R. G., Sana, H., & de Koter, A. 2013, *ApJ*, 764, 166, doi: [10.1088/0004-637X/764/2/166](https://doi.org/10.1088/0004-637X/764/2/166)
- Ekström, S., Georgy, C., Eggenberger, P., et al. 2012, *A&A*, 537, A146, doi: [10.1051/0004-6361/201117751](https://doi.org/10.1051/0004-6361/201117751)
- Eldridge, J. J., Langer, N., & Tout, C. A. 2011, *MNRAS*, 414, 3501, doi: [10.1111/j.1365-2966.2011.18650.x](https://doi.org/10.1111/j.1365-2966.2011.18650.x)
- Eldridge, J. J., & Stanway, E. R. 2012, *MNRAS*, 419, 479, doi: [10.1111/j.1365-2966.2011.19713.x](https://doi.org/10.1111/j.1365-2966.2011.19713.x)
- Evans, F. A., Renzo, M., & Rossi, E. M. 2020, arXiv e-prints, arXiv:2006.00849.  
<https://arxiv.org/abs/2006.00849>
- Farmer, R. 2018, *rjfarmer/mesaplot*, doi: [10.5281/zenodo.1441329](https://doi.org/10.5281/zenodo.1441329)
- Ferguson, J. W., Alexander, D. R., Allard, F., et al. 2005, *ApJ*, 623, 585, doi: [10.1086/428642](https://doi.org/10.1086/428642)
- Fuller, G. M., Fowler, W. A., & Newman, M. J. 1985, *ApJ*, 293, 1, doi: [10.1086/163208](https://doi.org/10.1086/163208)
- Fuller, J., Piro, A. L., & Jermyn, A. S. 2019, *MNRAS*, 485, 3661, doi: [10.1093/mnras/stz514](https://doi.org/10.1093/mnras/stz514)
- Gilkis, A., Vink, J. S., Eldridge, J. J., & Tout, C. A. 2019, *MNRAS*, 486, 4451, doi: [10.1093/mnras/stz1134](https://doi.org/10.1093/mnras/stz1134)
- Gordon, K. D., Gies, D. R., Schaefer, G. H., et al. 2018, *ApJ*, 869, 37, doi: [10.3847/1538-4357/aaec04](https://doi.org/10.3847/1538-4357/aaec04)
- Götberg, Y., de Mink, S. E., & Groh, J. H. 2017.  
<https://arxiv.org/abs/1701.07439>
- Götberg, Y., de Mink, S. E., Groh, J. H., et al. 2018, *A&A*, 615, A78, doi: [10.1051/0004-6361/201732274](https://doi.org/10.1051/0004-6361/201732274)
- Grasha, K., Roy, A., Sutherland, R. S., & Kewley, L. J. 2021, *ApJ*, 908, 241, doi: [10.3847/1538-4357/abd6bf](https://doi.org/10.3847/1538-4357/abd6bf)
- Grevesse, N., & Sauval, A. J. 1998, *SSRv*, 85, 161, doi: [10.1023/A:1005161325181](https://doi.org/10.1023/A:1005161325181)
- Heger, A., Langer, N., & Woosley, S. E. 2000, *ApJ*, 528, 368
- Hellings, P. 1983, *Ap&SS*, 96, 37, doi: [10.1007/BF00661941](https://doi.org/10.1007/BF00661941)  
—. 1984, *Ap&SS*, 104, 83, doi: [10.1007/BF00653994](https://doi.org/10.1007/BF00653994)
- Herrero, A., Kudritzki, R. P., Vilchez, J. M., et al. 1992, *A&A*, 261, 209
- Herwig, F. 2000, *A&A*, 360, 952

- Hirai, R., Podsiadlowski, P., & Yamada, S. 2018.  
<https://arxiv.org/abs/1803.10808>
- Hoogerwerf, R., de Bruijne, J. H. J., & de Zeeuw, P. T. 2000, ApJL, 544, L133, doi: [10.1086/317315](https://doi.org/10.1086/317315)
- . 2001, A&A, 365, 49, doi: [10.1051/0004-6361:20000014](https://doi.org/10.1051/0004-6361:20000014)
- Hunter, J. D. 2007, Computing In Science & Engineering, 9, 90
- Iglesias, C. A., & Rogers, F. J. 1993, ApJ, 412, 752, doi: [10.1086/172958](https://doi.org/10.1086/172958)
- . 1996, ApJ, 464, 943, doi: [10.1086/177381](https://doi.org/10.1086/177381)
- Itoh, N., Hayashi, H., Nishikawa, A., & Kohyama, Y. 1996, ApJS, 102, 411, doi: [10.1086/192264](https://doi.org/10.1086/192264)
- Kalogera, V. 1996, ApJ, 471, 352, doi: [10.1086/177974](https://doi.org/10.1086/177974)
- Kippenhahn, R., Ruschenplatt, G., & Thomas, H.-C. 1980, A&A, 91, 175
- Kippenhahn, R., & Weigert, A. 1967, ZA, 65, 251
- Klencki, J., Nelemans, G., Istrate, A. G., & Chruslinska, M. 2021, A&A, 645, A54, doi: [10.1051/0004-6361/202038707](https://doi.org/10.1051/0004-6361/202038707)
- Klencki, J., Nelemans, G., Istrate, A. G., & Pols, O. 2020, A&A, 638, A55, doi: [10.1051/0004-6361/202037694](https://doi.org/10.1051/0004-6361/202037694)
- Kolb, U., & Ritter, H. 1990, A&A, 236, 385
- Lagae, C., Driessen, F. A., Hennicker, L., Kee, N. D., & Sundqvist, J. O. 2021, arXiv e-prints, arXiv:2103.15904.  
<https://arxiv.org/abs/2103.15904>
- Langanke, K., & Martínez-Pinedo, G. 2000, Nuclear Physics A, 673, 481, doi: [10.1016/S0375-9474\(00\)00131-7](https://doi.org/10.1016/S0375-9474(00)00131-7)
- Langer, N. 1998, A&A, 329, 551
- Langer, N., Fricke, K. J., & Sugimoto, D. 1983, A&A, 126, 207
- Laplace, E., Götberg, Y., de Mink, S. E., Justham, S., & Farmer, R. 2020, A&A, 637, A6, doi: [10.1051/0004-6361/201937300](https://doi.org/10.1051/0004-6361/201937300)
- Laplace, E., Justham, S., Renzo, M., et al. 2021, arXiv e-prints, arXiv:2102.05036.  
<https://arxiv.org/abs/2102.05036>
- Law-Smith, J. A. P., Everson, R. W., Ramirez-Ruiz, E., et al. 2020, arXiv e-prints, arXiv:2011.06630.  
<https://arxiv.org/abs/2011.06630>
- Lubow, S. H., & Shu, F. H. 1975, ApJ, 198, 383, doi: [10.1086/153614](https://doi.org/10.1086/153614)
- Lucy, L. B. 2012, A&A, 544, A120, doi: [10.1051/0004-6361/201118753](https://doi.org/10.1051/0004-6361/201118753)
- Maeder, A., & Meynet, G. 2000, ARA&A, 38, 143, doi: [10.1146/annurev.astro.38.1.143](https://doi.org/10.1146/annurev.astro.38.1.143)
- Marcolino, W. L. F., Bouret, J. C., Martins, F., et al. 2009, A&A, 498, 837, doi: [10.1051/0004-6361/200811289](https://doi.org/10.1051/0004-6361/200811289)
- Mason, B. D., Hartkopf, W. I., Gies, D. R., Henry, T. J., & Helsel, J. W. 2009, AJ, 137, 3358, doi: [10.1088/0004-6256/137/2/3358](https://doi.org/10.1088/0004-6256/137/2/3358)
- Meynet, G., & Maeder, A. 2000, A&A, 361, 101 —. 2003, A&A, 404, 975, doi: [10.1051/0004-6361:20030512](https://doi.org/10.1051/0004-6361:20030512)
- Morton, D. C. 1960, ApJ, 132, 146, doi: [10.1086/146908](https://doi.org/10.1086/146908)
- Murphy, S. J., Joyce, M., Bedding, T. R., White, T. R., & Kama, M. 2021, MNRAS, 502, 1633, doi: [10.1093/mnras/stab144](https://doi.org/10.1093/mnras/stab144)
- Neo, S., Miyaji, S., Nomoto, K., & Sugimoto, D. 1977, PASJ, 29, 249
- Neugent, K. F., Massey, P., Hillier, D. J., & Morrell, N. 2017, ApJ, 841, 20, doi: [10.3847/1538-4357/aa6e51](https://doi.org/10.3847/1538-4357/aa6e51)
- Neuhäuser, R., Gießler, F., & Hambaryan, V. V. 2020, MNRAS, 498, 899, doi: [10.1093/mnras/stz2629](https://doi.org/10.1093/mnras/stz2629)
- Oda, T., Hino, M., Muto, K., Takahara, M., & Sato, K. 1994, Atomic Data and Nuclear Data Tables, 56, 231, doi: [10.1006/adnd.1994.1007](https://doi.org/10.1006/adnd.1994.1007)
- Packet, W. 1981, A&A, 102, 17
- Paczynski, B. 1991, ApJ, 370, 597, doi: [10.1086/169846](https://doi.org/10.1086/169846)
- Paxton, B., Bildsten, L., Dotter, A., et al. 2011, ApJS, 192, 3, doi: [10.1088/0067-0049/192/1/3](https://doi.org/10.1088/0067-0049/192/1/3)
- Paxton, B., Cantiello, M., Arras, P., et al. 2013, ApJS, 208, 4, doi: [10.1088/0067-0049/208/1/4](https://doi.org/10.1088/0067-0049/208/1/4)
- Paxton, B., Marchant, P., Schwab, J., et al. 2015, ApJS, 220, 15, doi: [10.1088/0067-0049/220/1/15](https://doi.org/10.1088/0067-0049/220/1/15)
- Paxton, B., Schwab, J., Bauer, E. B., et al. 2018, ApJS, 234, 34, doi: [10.3847/1538-4365/aaa5a8](https://doi.org/10.3847/1538-4365/aaa5a8)
- Paxton, B., Smolec, R., Gautschy, A., et al. 2019.  
<https://arxiv.org/abs/1903.01426>
- Pérez, F., & Granger, B. E. 2007, Computing in Science & Engineering, 9, 21
- Perna, R., Duffell, P., Cantiello, M., & MacFadyen, A. I. 2014, ApJ, 781, 119, doi: [10.1088/0004-637X/781/2/119](https://doi.org/10.1088/0004-637X/781/2/119)
- Podsiadlowski, P. 2003, arXiv e-prints, astro.  
<https://arxiv.org/abs/astro-ph/0303660>
- Pols, O. R., & Marinus, M. 1994, A&A, 288, 475
- Pols, O. R., Tout, C. A., Eggleton, P. P., & Han, Z. 1995, MNRAS, 274, 964, doi: [10.1093/mnras/274.3.964](https://doi.org/10.1093/mnras/274.3.964)
- Popham, R., & Narayan, R. 1991, ApJ, 370, 604, doi: [10.1086/169847](https://doi.org/10.1086/169847)
- Potekhin, A. Y., & Chabrier, G. 2010, Contributions to Plasma Physics, 50, 82, doi: [10.1002/ctpp.201010017](https://doi.org/10.1002/ctpp.201010017)
- Przybilla, N., Nieva, M. F., Heber, U., & Butler, K. 2008, The Astrophysical Journal, 684, L103, doi: [10.1086/592245](https://doi.org/10.1086/592245)
- Qin, Y., Fragos, T., Meynet, G., et al. 2018, A&A, 616, A28, doi: [10.1051/0004-6361/201832839](https://doi.org/10.1051/0004-6361/201832839)
- Rain, M. J., Ahumada, J., & Carraro, G. 2021, arXiv e-prints, arXiv:2103.06004.  
<https://arxiv.org/abs/2103.06004>
- Renzo, M., Ott, C. D., Shore, S. N., & de Mink, S. E. 2017, A&A, 603, A118, doi: [10.1051/0004-6361/201730698](https://doi.org/10.1051/0004-6361/201730698)

- Renzo, M., Zapartas, E., de Mink, S. E., et al. 2019, A&A, 624, A66, doi: [10.1051/0004-6361/201833297](https://doi.org/10.1051/0004-6361/201833297)
- Rogers, F. J., & Nayfonov, A. 2002, ApJ, 576, 1064, doi: [10.1086/341894](https://doi.org/10.1086/341894)
- Sana, H., de Mink, S. E., de Koter, A., et al. 2012, Science, 337, 444, doi: [10.1126/science.1223344](https://doi.org/10.1126/science.1223344)
- Saumon, D., Chabrier, G., & van Horn, H. M. 1995, ApJS, 99, 713, doi: [10.1086/192204](https://doi.org/10.1086/192204)
- Schneider, F. R. N., Podsiadlowski, P., Langer, N., Castro, N., & Fossati, L. 2016, MNRAS, 457, 2355, doi: [10.1093/mnras/stw148](https://doi.org/10.1093/mnras/stw148)
- Schneider, F. R. N., Podsiadlowski, P., & Müller, B. 2021, A&A, 645, A5, doi: [10.1051/0004-6361/202039219](https://doi.org/10.1051/0004-6361/202039219)
- Schootemeijer, A., Langer, N., Grin, N. J., & Wang, C. 2019, A&A, 625, A132, doi: [10.1051/0004-6361/201935046](https://doi.org/10.1051/0004-6361/201935046)
- Sota, A., Maíz Apellániz, J., Morrell, N. I., et al. 2014, ApJS, 211, 10, doi: [10.1088/0067-0049/211/1/10](https://doi.org/10.1088/0067-0049/211/1/10)
- Spruit, H. C. 2002, A&A, 381, 923, doi: [10.1051/0004-6361:20011465](https://doi.org/10.1051/0004-6361:20011465)
- Sravan, N., Marchant, P., & Kalogera, V. 2019, ApJ, 885, 130, doi: [10.3847/1538-4357/ab4ad7](https://doi.org/10.3847/1538-4357/ab4ad7)
- Suda, T., Saitoh, T. R., Moritani, Y., Matsuno, T., & Shigeyama, T. 2021, arXiv e-prints, arXiv:2103.13627. <https://arxiv.org/abs/2103.13627>
- Sweet, P. A. 1950, MNRAS, 110, 548, doi: [10.1093/mnras/110.6.548](https://doi.org/10.1093/mnras/110.6.548)
- Tauris, T. M. 2015, MNRAS, 448, L6, doi: [10.1093/mnrasl/slu189](https://doi.org/10.1093/mnrasl/slu189)
- Tauris, T. M., & Takens, R. J. 1998, A&A, 330, 1047
- Tauris, T. M., Kramer, M., Freire, P. C. C., et al. 2017, ApJ, 846, 170, doi: [10.3847/1538-4357/aa7e89](https://doi.org/10.3847/1538-4357/aa7e89)
- Tetzlaff, N., Neuhäuser, R., Hohle, M. M., & Maciejewski, G. 2010, MNRAS, 402, 2369, doi: [10.1111/j.1365-2966.2009.16093.x](https://doi.org/10.1111/j.1365-2966.2009.16093.x)
- Timmes, F. X., & Swesty, F. D. 2000, ApJS, 126, 501, doi: [10.1086/313304](https://doi.org/10.1086/313304)
- Townsend, R. 2018, MESA SDK for Linux: 20180822, doi: [10.5281/zenodo.2603170](https://doi.org/10.5281/zenodo.2603170)
- Ulrich, R. K., & Burger, H. L. 1976, ApJ, 206, 509, doi: [10.1086/154406](https://doi.org/10.1086/154406)
- van der Walt, S., Colbert, S. C., & Varoquaux, G. 2011, Computing in Science Engineering, 13, 22, doi: [10.1109/MCSE.2011.37](https://doi.org/10.1109/MCSE.2011.37)
- van Rensbergen, W., de Greve, J. P., Mennekens, N., Jansen, K., & de Loore, C. 2011, A&A, 528, A16, doi: [10.1051/0004-6361/201015596](https://doi.org/10.1051/0004-6361/201015596)
- van Rensbergen, W., De Loore, C., & Jansen, K. 2006, A&A, 446, 1071, doi: [10.1051/0004-6361:20053543](https://doi.org/10.1051/0004-6361:20053543)
- van Rensbergen, W., Vanbeveren, D., & De Loore, C. 1996, A&A, 305, 825
- Vartanyan, D., Laplace, E., Renzo, M., et al. 2021, arXiv e-prints, arXiv:2104.03317. <https://arxiv.org/abs/2104.03317>
- Villamariz, M. R., & Herrero, A. 2005, A&A, 442, 263, doi: [10.1051/0004-6361:20052848](https://doi.org/10.1051/0004-6361:20052848)
- Vinciguerra, S., Neijssel, C. J., Vigna-Gómez, A., et al. 2020, MNRAS, 498, 4705, doi: [10.1093/mnras/staa2177](https://doi.org/10.1093/mnras/staa2177)
- Vink, J. S., Davies, B., Harries, T. J., Oudmaijer, R. D., & Walborn, N. R. 2009, A&A, 505, 743, doi: [10.1051/0004-6361/200912610](https://doi.org/10.1051/0004-6361/200912610)
- Vink, J. S., de Koter, A., & Lamers, H. J. G. L. M. 2000, A&A, 362, 295  
—. 2001, A&A, 369, 574, doi: [10.1051/0004-6361:20010127](https://doi.org/10.1051/0004-6361:20010127)
- Walker, G. A. H., Yang, S., & Fahlman, G. G. 1979, ApJ, 233, 199, doi: [10.1086/157381](https://doi.org/10.1086/157381)
- Wang, C., Langer, N., Schootemeijer, A., et al. 2020, ApJL, 888, L12, doi: [10.3847/2041-8213/ab6171](https://doi.org/10.3847/2041-8213/ab6171)
- Wheeler, J. C., Lecar, M., & McKee, C. F. 1975, ApJ, 200, 145, doi: [10.1086/153771](https://doi.org/10.1086/153771)
- Yoon, S.-C., Dessart, L., & Clocchiatti, A. 2017, ApJ, 840, 10, doi: [10.3847/1538-4357/aa6afe](https://doi.org/10.3847/1538-4357/aa6afe)
- Yoon, S.-C., Langer, N., & Norman, C. 2006, A&A, 460, 199, doi: [10.1051/0004-6361:20065912](https://doi.org/10.1051/0004-6361:20065912)
- Zahn, J. P. 1992, A&A, 265, 115
- Zaldarriaga, M., Kushnir, D., & Kollmeier, J. A. 2018, MNRAS, 473, 4174, doi: [10.1093/mnras/stx2577](https://doi.org/10.1093/mnras/stx2577)
- Zapartas, E., de Mink, S. E., Justham, S., et al. 2021, A&A, 645, A6, doi: [10.1051/0004-6361/202037744](https://doi.org/10.1051/0004-6361/202037744)  
—. 2019. <https://arxiv.org/abs/1907.06687>
- Zehe, T., Mugrauer, M., Neuhäuser, R., et al. 2018, Astronomische Nachrichten, 339, 46, doi: [10.1002/asna.201713383](https://doi.org/10.1002/asna.201713383)